Revision: 2

Title: Visible-Infrared Spectral Properties of Iron-bearing Aluminate Spinel Under Lunar-like Redox Conditions

Authors: Colin R.M. Jackson, Leah C. Cheek, Kelsey B. Williams, Kerri Donaldson Hanna, Carle M. Pieters, Stephen W. Parman, Reid F. Cooper, Darby Dyar, Melissa Nelms, Mark R. Salvatore

Originally submitted to American Mineralogist, Lunar Highlands Special Issue, October 2013
Resubmitted to American Mineralogist, Lunar Highlands Special Issue, February 2014

ABSTRACT

Remote sensing observations have identified aluminate spinel, in the absence of measureable olivine and pyroxene, as a globally distributed component of the lunar crust. Earlier remote sensing observations and returned samples did not indicate the presence of this component, leaving its geologic significance unclear. Here, we report visible to mid-infrared (V-IR) reflectance (300-25000 nm) and Mössbauer spectra of aluminate spinels, synthesized at lunar-like oxygen fugacity (fO_2), that vary systematically in Fe abundance. Reflectance spectra of particulate (<45 μm), nominally stoichiometric aluminate spinels display systematic behavior, with bands at 700, 1000, 2000, and 2800 nm increasing in strength with increasing bulk Fe content. The especially strong bands at 2000 and 2800 are discernible for all spinel compositions

and saturate at <15 Fe# (Fe/(Mg+Fe)×100, molar). Absorption bands at 700 and 1000 nm, collectively referred to as the 1000 nm bands, are weaker and become observable at >6 Fe#. Although the 2000 and 2800 nm bands are assigned to Fe_{IV}^{+2} electronic transitions, spectra of aluminate spinels with excess Al_2O_3 demonstrate that the strengths of the 1000 nm bands are related to the abundance of Fe_{VI}^{+2}. The abundance of Fe_{VI}^{+2} depends on bulk Fe content as well as factors that control the degree of structural order-disorder, such as cooling rate. Consequently the strength of the 1000 nm bands are useful for constraining the Fe content and cooling rate of remotely sensed spinel. Controlling for cooling rate, particle size, and fO_2, we conclude that spinels with >12 Fe# (<88 Mg#) have observable 1000 nm bands under ambient lunar conditions and that only very Mg-rich spinels lack 1000 nm bands in their spectra. This links remote observations of spinel anorthosite to Mg-Suite magmatism. The combined effects of Fe oxidation state, abundance of co-existing plagioclase, and space weathering have not been explored here, and may add additional constraints. The relative strengths of the distinctive 1000 and 2000 nm bands of the spinels associated with pyroclastic deposits at Sinus Aestuum suggest fast cooling rates, possibly in the absence of an extensive vapor cloud.

INTRODUCTION

Recent observations by the Moon Mineralogy Mapper (M^3) and SELENE Spectral Profiler have identified aluminate spinel (i.e. $(Mg,Fe)Al_2O_4$-rich spinel) in exposures distributed globally across the lunar surface (Pieters et al., 2011; Dhingra et al., 2011; Dhingra and Pieters, 2011; Bhattacharya et al., 2012; Kaur et al., 2012; Lal et al., 2012; Yamamoto et al., 2013; Pieters et al., 2014). These identifications are based on the occurrence of strong absorption

bands near 2000 and 2800 nm in reflectance spectra that are diagnostic of ferrous iron situated in tetrahedral coordination (i.e. Fe_{IV}^{+2}) within a spinel lattice (e.g. Cloutis et al., 2004). In many of these identifications aluminate spinel is the only observable mineral using visible to near-infrared (V-NIR) remote sensing techniques, suggesting low proportions of the mafic silicates. Analogous materials with aluminate spinel as the dominant Fe-bearing phase have not been found in lunar samples from the Apollo and Luna missions, nor in lunar meteorites, leaving the petrogenesis and geologic significance of these new observations unclear.

Distinguishing between various new formation hypotheses (discussed below) for these spinel-bearing materials is challenging without information about the composition of the observed spinels. In particular, estimates of spinel Fe# (Fe/(Mg+Fe)×100, molar, 100-Mg#) are useful for constraining the composition of parental liquids involved in their formation. Importantly, laboratory analyses of spinel V-NIR spectra have shown that while strong absorptions at wavelengths >2000 nm are common for nearly all spinel compositions (and are therefore useful for spinel identification), additional absorptions at <1000 nm may also be apparent only for spinel with more than a few weight percent Fe (Cloutis et al., 2004). Thus, observations of V-NIR characteristics near 1000 nm in spinel spectra may provide significant leverage for estimating spinel Fe#. However, the specific causes of the <1000 nm absorptions and the nature of their dependence on Fe# have remained difficult to define and are the focus of the current work.

Here, we present a coordinated analysis of <1000 nm absorption strengths and Fe# using spinel samples that are synthesized at lunar-like conditions. This work builds upon the study by Cloutis et al. (2004) that characterized spectra of natural terrestrial spinels and aims to better resolve the observed relationship between spinel spectral characteristics and mineral

composition. Specifically, we 1) analyze the change in absorption strengths for spinels of various bulk Fe contents produced under identical conditions, and 2) characterize these results in terms of other factors (Al_2O_3 activity, cooling rate) that control the partitioning of Fe between the octahedral and tetrahedral crystallographic sites. This dataset, in combination with theoretical considerations, serves as a basis to constrain the Fe content and cooling rate of spinels recently identified in remotely sensed data. This information provides additional context for petrogenetic hypotheses regarding spinel deposits and additional insight into the magmatic history of the Moon.

ORIGIN OF SPINEL V-NIR ABSORPTIONS

The dominant features in spectra of normal spinels are the strong 2000 and 2800 nm absorptions owing to Fe_{IV}^{+2} (e.g. Cloutis et al., 2004). However, crystal field theory also predicts that Fe_{VI}^{+2} should generate absorption bands near 1000 nm associated with a $^5T_2$-^5E electron transition (e.g. Mao and Bell, 1975; Dickson and Smith, 1976). Similarly, crystal field theory predicts Fe_{IV}^{+2} is responsible for a series of bands near 700 nm (Gaffney, 1973; Mao and Bell, 1975). A study of absorption properties of synthetic aluminate spinel, however, produced linear correlations between the product of octahedral divalent and trivalent Fe concentration ($[Fe_{VI}^{+2}]\times[Fe_{VI}^{+3}]$) and the net linear extinction coefficients at ~700 and ~1000 nm (Halenius et al., 2002). These observations, in combination with the general spectral shape and band positions, were used to argue that the bands at ~700 and 1000 nm are caused by exchanged-coupled pair transitions and intervalence charge transfers, respectively. More recently, it has been argued that bands at ~700 and 1000 nm are caused by spin-forbidden transitions of Fe_{VI}^{+3} based on observed pressure and temperature systematics of spinel spectra (Taran et al., 2005).

Importantly, the strength of bands near 1000 nm in the latter two mechanisms depends on the abundance of Fe^{+3}, which is relatively scarce given the reduced nature of lunar rocks (e.g. Sato et al., 1973; Delano, 1990; Fogel and Rutherford, 1995; Karner et al., 2006). Thus, lunar spinels may require relatively large concentrations of total Fe in order to generate prominent bands near 1000 nm. Moreover, $[Fe_{VI}^{+2}]$ is related the degree of ordering in spinel (e.g. Harrison et al., 1998), which is uncertain for remotely sensed samples. Thus, a primary objective of this study is to determine the V-IR (300-25000 nm) spectral properties of synthetic spinel under the environmental conditions (e.g. fO_2 and cooling rate) applicable to the Moon.

REMOTE IDENTIFICATION OF SPINEL ON THE MOON

Aluminate spinel identifications on the Moon can be divided into two general categories, here termed Group 1 and Group 2, based on observed geologic context and V-NIR characteristics. Group 1 identifications are associated with basin walls or large craters (see summary in Pieters et al., 2014). These structural units are thought to represent materials uplifted from significant depth (Cintala and Grieve, 1998), suggesting an origin related to the deep crust. Characteristic spectra of Group 1 lithologies display a strong absorption centered at 2000 nm but little to no associated structure at shorter wavelengths in the V-NIR spectral range (500-1000 nm). Olivine and pyroxene have characteristic absorption bands near 1000 nm (Burns, 1970; Adams, 1974), suggesting mafic silicates are absent or are only a minor component of these aluminate spinel-bearing units. Spinel can also absorb radiation near 1000 nm, but such spectral features are associated with relatively high Fe/Mg and/or Cr/Al ratios (Cloutis et al., 2004). Thus, the lack of absorption features near 1000 nm suggests the spinel-bearing rock observed in

Group 1 is a Mg-rich, Fe-poor aluminate spinel anorthosite. The presence of plagioclase is supported by the relatively high albedo the regions associated with Group 1 and the observation that their surrounding host material is highly anorthositic (Pieters et al., 2014).

Group 2 identifications are associated with dark mantle deposits (DMDs) at Sinus Aestuum (Sunshine et al., 2010, Yamamoto et al., 2013). It is hypothesized that these spinels were transported to the lunar surface through pyroclastic eruptions and are not associated with impact structures. Characteristic V-NIR spectra of Group 2 are distinctive from Group 1. Specifically, the continuum-corrected spectra of spinels associated with the DMDs of Sinus Aestuum have a doublet absorption band, with minima near 700 and 1000 nm, in addition to a prominent band centered near 2000 nm. The doublet band at shorter wavelengths is associated with aluminate spinels that are relatively rich in Fe (e.g. Cloutis et al., 2004), suggesting that the DMD spinels of Sinus Aestuum are distinctly richer in Fe compared to the spinels associated with Group 1 (Yamamoto et al., 2013).

Following the identification of aluminate spinel associated with basin walls and large craters (Group 1), several hypotheses for the formation of spinel anorthosite have been advanced. These include fractional crystallization-assimilation of anorthositic country rock by picritic liquids (Gross and Treiman, 2011), reaction between Mg-Suite parental liquids and anorthositic crust (Prissel et al., 2014), and fractional crystallization of a plagioclase-rich impact melt (Vaughan et al., 2013). Group 1 spinel deposits have also been proposed to be possibly exogenic, derived from relatively slow colliding impactors (Yue et al., 2013). The aluminate spinels associated with DMDs (Group 2) have been proposed to be derived from fire-fountain eruptions of relatively Fe-rich picritic liquids with high normative plagioclase as a result of melt-wallrock interactions in the lunar crust (Yamamoto et al., 2013). Evaluating formation

hypotheses requires a systematic understanding of the major controls on spinel absorption characteristics in order to place compositional constraints on these spinel-bearing materials. Toward this goal, the current work focuses on a detailed characterization of 1000 nm absorption band strengths as a function of both Fe# as well as partitioning of Fe among different crystallographic sites.

METHODS

Mineral synthesis

Three series of spinels were synthesized: (1) FeSp6, which investigates the effect of varying Fe#, (2) FeSp8, which incorporates excess alumina, and (3) FeSp10, which tests the effect of cooling rate on spectral properties. The Fe# series (FeSp6) is the primary focus of this work, whereas the cooling rate experiment (FeSp10) consists of one sample and is intended to demonstrate the effects of partitioning between different crystallographic sites. The series investigating the effects of excess alumina (FeSp8) also characterizes the effects of partitioning, but, more importantly, is used to demonstrate that the <1000 nm bands in spinel are related to $[Fe^{+2}_{VI}]$.

For the FeSp6 series, reagent grade oxides (MgO, Fe_2O_3, and Al_2O_3) were mixed in stoichiometric proportions to form aluminate spinel. Ten different starting compositions were produced that vary systematically in Fe# from ~0 to 32. Oxides were homogenized using an agate mortar and pestle under ethanol. The dry powders were mixed with polyvinyl alcohol to provide additional binding strength and then pressed into 1 cm diameter compacts (~1 cm height). Compacts were then placed on a bed of zirconia beads (~1 mm in diameter) contained

by an alumina boat and loaded into a horizontal gas-mixing furnace. Sintering durations were 72 hours and temperatures were 1450°C. Oxygen fugacity was fixed by streaming a CO-CO_2 mixture through the furnace. The necessary CO/CO_2 ratio for a given fO_2 was determined using yittra-doped zirconia fO_2 sensor, but fO_2 was not actively monitored for the duration of sintering. After sintering, the temperature was ramped down to room temperature over approximately 6 hours, for an integrated cooling rate of ~$5x10^{-2}$ °C s^{-1}.

The FeSp8 series was produced following the same procedure as above, using surplus powder from select FeSp6 starting compositions with additional Al_2O_3 (2.5-7.5 wt. %) added to document the effect of point defect chemistry on V-NIR spectra (see V-NIR $a Al_2O_3$ section). The stoichiometry calculated for the FeSp8 spinels supports presence of excess Al_2O_3 in FeSp8 spinels (Appendix Table 1). The FeSp10 series is comprised of a single experiment that was conducted using a vertical gas-mixing furnace configured for rapid quenching of samples. In this furnace, a compact is suspended in the hotspot by platinum (Pt) hooks and a Pt basket. The sample is drop quenched in water by passing a current through and melting a thin Pt wire that connects the basket and hooks. The starting oxides for the FeSp10 compact were taken from surplus FeSp6_11 powders. Duration and fO_2 were the same as for the FeSp6 and FeSp8 experiments, but temperature was 1400 °C. Fragments of the sintered compacts were mounted for major element analysis by electron microprobe, and the remainder was crushed and dry sieved into particle size separates for V-IR, Mössbauer, and Flux Fusion analysis. Particle size separate were <45 μm, 45-75 μm, 75-125 μm.

Electron microprobe analysis

Major element compositions of the sintered spinels were determined using an electron microprobe (Cameca SX-100, Brown University). Analyses were completed using wavelength dispersive spectrometry, and the PAP correction was applied. The analytical parameters were 15 kV, 20 nA, and a focused beam. Counting times on all elements were 45 seconds, excepting Fe (90 seconds). Internal standards of a stoichiometric spinel *sensu stricto* (*ss*, $MgAl_2O_4$) and Fe-bearing spinel were analyzed between samples to correct for any drift over the course of the analytical sessions. Spot locations were distributed throughout each sample to document any compositional heterogeneity.

Flux Fusion analysis

Inductively coupled plasma-atomic emission spectroscopy (ICP-AES) was utilized to measure the bulk chemistry of the FeSp6 series spinels in a fashion similar to that described in Murray et al. (2000). Forty milligram sample aliquots were sieved to particle sizes < 125 μm and combined with a flux composed of 160 mg $LiBO_2$. The mixture was then fused for 15 minutes at 1050 ºC; because of the high melting temperature of spinel and the absence of volatile components, the fusion duration was extended from the traditional 10 minutes (as discussed in Murray et al., 2000) to 15 minutes. Following fusion, the melts were quenched in 20 mL of 10% HNO_3 and agitated for one hour. Over the hour duration the quench bead dissolved into the HNO_3 solution. The solutions were then filtered through 0.45 μm filters and diluted in additional 10% HNO_3 for analysis. A JY2000 Ultrace ICP Atomic Emission Spectrometer was used to perform elemental analyses on the diluted samples and analyzed for Al, Ca, Cr, Fe, Mg, Ni, Si, and Ti using a Gaussian peak search technique. Intensity measurements were calibrated and converted to geologically relevant units using a series of blanks and geochemical standards that

were processed simultaneously and in the same fashion as the samples. All samples, standards, and blanks were run in duplicate, at minimum, to increase the robustness of the measurements and to ensure the reproducibility of the results.

Six replicates of FeSp6_10 were measured to provide an estimate of the precision of our flux fusion analysis. The average Fe# for FeSp6_10 was 25.06 ± 0.28 % (95% confidence). Average yield on all flux fusion analyses was 97.63 ± 8.78 % (95% confidence), neglecting a single outlier (outlier yield = 69.0 %), indicating complete or nearly complete dissolution of the spinel into the flux. The outlier Fe# (10.25 Fe#) is similar to the duplicate Fe# (10.26 Fe#) run on the same sample.

Reflectance spectroscopy

In preparation for the reflectance measurements, samples were dry sieved to a uniform particle size of <45 μm and loaded into 9-mm diameter Teflon-coated sample dishes. Reflectance spectra were acquired in RELAB at Brown University using both the Bidirectional Reflectance spectrometer (BDR) (300 – 2600 nm), which measures V-NIR wavelengths and the Thermo Nicolet Nexus 870 Fourier-Transform infrared spectrometer (FTIR) (800-25000 nm), which measures out to mid-infrared wavelengths. All BDR spectra were acquired with an incidence angle of 30° and a 0° emergence angle (Pieters and Hiroi, 2004). Following conventional RELAB procedures, the BDR and FTIR data were spliced near 1000 nm by adjusting the reflectance scale of the FTIR data to the BDR data using a multiplicative factor. The connecting wavelength was chosen so that the two spectra connect smoothly with similar inclinations. Larger particle size fractions (45-75 and 75-125 μm) were also measured for select samples. All reflectance spectra will be available through the RELAB archive.

The strengths of the V-NIR bands are expected to increase with increasing Fe abundance in the spinel, as described above. To measure this effect for the bands at 1000, 2000, and 2800 nm, the spectra for all samples were first scaled so that the reflectance maximum between 1000-2000 nm (determined by a polynomial fit) equaled one. This procedure effectively minimizes albedo variations among samples in order to facilitate comparison of band strengths, making a further continuum removal unnecessary. A second-degree polynomial was then fit, in a least squares sense, between 825-1100 nm, 1700-2200 nm, and 2700-3000 nm, and minimum reflectance value for each polynomial was identified. The minimum reflectance value for each polynomial is expected to negatively correlate with the concentration of the cation species responsible for the band. The natural log of the reflectance minimum ($\ln(\text{reflectance}_{min})$) for each band was then calculated. We term the slope of proportionality between the natural log of the reflectance minimum and the concentration of the cation species responsible for the band a "reflectance coefficient."

Across the mid-infrared (mid-IR) spectral range (1250 – 400 cm^{-1} or 8000 – 25000 nm), radiation is commonly measured and reported in terms of emissivity, which can be approximated from our data by subtracting the measured reflectance values from one (Hapke, 1993). For the following discussions we report the mid-IR spectra in this way to facilitate comparison with previous laboratory studies. The primary spectral features in the mid-IR are 1) the Christiansen feature (CF), an emissivity maximum between ~900 – 1000 cm^{-1} (with a secondary CF between ~550 – 650 cm^{-1}) that is often diagnostic of mineralogy and average composition (Conel, 1969), and 2) the restsrahlen bands (RB), which occur between ~650 – 850 cm^{-1} and ~400 – 650 cm^{-1} and represent molecular vibrations related to stretching and bending motions. To determine the frequency (cm^{-1}) of these spectral features, a second degree polynomial was fit to each spectral

253 feature in each spectrum following the approach used to calculate band positions in the V-NIR
254 spectral region. Laboratory studies have shown that the CF systematically shifts according to
255 Mg# and An# for olivine and plagioclase feldspar, respectively (e.g. Hamilton, 2010; Donaldson
256 Hanna et al., 2012). Thus to determine the frequency of the CF for each spinel sample a
257 polynomial was fit to a portion of the ~900 – 1000 cm^{-1} spectral range of each spectrum and the
258 frequency of the maximum emissivity value in the polynomial fit was used to represent the CF
259 position. The same method was used to find the position of the secondary CF in the ~550 – 650
260 cm^{-1} spectral range. Diagnostic absorptions in the RB are also fit to determine frequencies at
261 which the emissivity minimum values are identified. The spectral range was varied in order to
262 best fit the emissivity and shape of the CF and each RB feature for each sample spectrum.
263 Goodness of fit between each polynomial and the measured emissivity spectrum was evaluated
264 using RMS values. Due to the non-unique nature of identifying the spectral features using this
265 methodology, the positions of spectral features can vary by ± 3 cm^{-1} as the spectral range and
266 polynomial order are changed (Donaldson Hanna et al., 2012). In wavelength space, a ± 3 cm^{-1}
267 error at ~7500 – 8000 nm equates to an error of ± 20 nm.
268
269 **Mössbauer analysis**
270 To determine the coordination state of Fe in each synthetic spinel sample, Mössbauer
271 data were collected for all samples from the FeSp6 and FeSp8 series, with the exception of the
272 nominally Fe-free FeSp6_1. Approximately 10-30 mg of each sample was mixed with sugar
273 under acetone before mounting in a sample holder confined by Kapton® polyimide film tape.
274 Mössbauer spectra were acquired at 22 ˚C using a WEB Research Co. model WT302
275 spectrometer (Mount Holyoke College) with a 100-60 mCi 57Co in Rh source. Results were

276 calibrated against a 25 μm α-Fe foil. Spectra were collected in 2048 channels and corrected for
277 nonlinearity via interpolation to a linear velocity scale, which is defined by the spectrum of the
278 25 μm Fe foil used for calibration. The WMOSS algorithm fits a straight line to the points
279 defined by the published values of the Fe metal peak positions (as y values) and the observed
280 positions in channels (x values). Data were then folded before fitting, using the WMOSS Auto-
281 fold procedure that folds the spectrum about the channel value that produces the minimum least
282 squares sum difference between the first half of the spectrum and the reflected second half of the
283 spectrum.

284 For each sample, the fraction of the baseline due to the Compton scattering of 122 keV
285 gammas by electrons inside the detector was determined by measuring the count rate with and
286 without a 14.4-keV stop filter (~2 mm of Al foil) in the gamma beam. Compton-corrected
287 absorption was calculated for each individual spectrum using the formulation A/(1 - b), where b
288 is the Compton fraction and A is the uncorrected absorption. This correction does not change the
289 results of the fits per se but does allow accurate determination of % absorption in the spectra. It
290 is necessary because the range of energy deposited in the detector by Compton events extends
291 from 0 keV to 40 keV, overlapping both the 14 keV and 2 keV energies deposited by the 14.4
292 keV gammas. Run times were 6-24 hours per spectrum, and baseline counts ranged from ~2.2 to
293 14.0 million after the Compton correction.

294 Spectra were fit with two or three Lorentzian doublets using the MEX_FielDD program
295 acquired from the University of Ghent courtesy of E. DeGrave. Center shifts (CS, or δ), and
296 quadrupole splittings (QS, or Δ) of the doublets were allowed to vary, and widths (full width at
297 half maximum) of all four peaks were coupled to vary in pairs. Errors on center shift and
298 quadrupole splitting of well-resolved peaks are usually ±0.02 mm/s in natural samples (e.g.,

Skogby et al. 1992), though these can be reduced by use of consistent sample preparation, run conditions, and fitting procedures to ± 0.005 mm/s. Reproducibility (precision) of peak areas based on repeated fits using different constraints (δ, Δ, width, and areas constrained in all possible combinations of individual peaks and pairs) and fitting models (Lorentzian, Gaussian, quadrupole splitting distributions) are ± 0.3% absolute for these well-resolved spectra; accuracy has been determined in previous analogous studies of amphiboles to be ± 3-5% (Dyar, 1989).

RESULTS

Sample descriptions and major element compositions

A backscattered image of a typical run product is shown in Figure 1. The samples contain both large scale porosity (~100 μm diameter) and small scale porosity (~1 μm diameter), as is typical for sintered products. Major element compositions of the synthesized spinels as determined by electron microprobe are provided in Appendix Table 1. The overwhelmingly dominant phase present is (Fe,Mg) aluminate spinel. Minor amounts of ferro-periclase were observed in some run products (noted in Appendix Table 1). Spot analysis showed some within-sample variability in the spinel Fe#, but this variability is minor compared to the full range of compositions synthesized (Appendix Table 1). Some electron microprobe analyses have low totals, presumably because the activated volume of spinel included a small porous component.

Flux fusion is a bulk analytical technique that averages out compositional heterogeneities and provides an effective composition for comparison with spectral signatures, which also represent bulk measurements. For this reason we choose to use the flux fusion determinations of Fe#, which are provided in Appendix Table 1, for inter-sample comparisons within the FeSp6

series. Absolute values of oxide abundances determined by flux fusion are not reported because the yields are deemed less reliable compared to electron microprobe analysis. For higher Fe samples, flux fusion and electron microprobe measurements agree in Fe# to within 20% and usually to within 10% (Appendix Table 1). For the lowest Fe samples (<3 Fe#), the disagreement between the two techniques can be larger on a percent basis due to increased uncertainties at such low concentrations of the species of interest.

Mössbauer - Distribution of ferric iron

Halenius et al. (2002) demonstrated a linear dependence between the strength of 700 and 1000 nm bands and $[Fe_{VI}^{+2}]\times[Fe_{VI}^{+3}]$ in spinel, suggesting Fe_{VI}^{+3} also contributes to the strength of short wavelength bands in the V-NIR spectral range. A comparison of Group B and C V-NIR spectra from Cloutis et al. (2004) also provides evidence that Fe_{VI}^{+3} contributes to the strength of the 700 and 1000 nm bands. The abundance of Fe_{VI}^{+3} in spinel is positively related to the fO_2 of the system, suggesting the 1000 nm bands could be relatively weak in lunar spinels for a given bulk Fe content because the Moon is a reducing environment compared to Earth's uppermost mantle and crust (e.g. Delano, 1990; Fogel and Rutherford, 1995; Karner et al., 2006; Sato et al., 1973).

The spinels presented here were synthesized under low fO_2 that is directly applicable to the Moon (IW-1). The abundance of Fe_{VI}^{+3} was measured by Mössbauer spectroscopy for samples from the Fe# series (FeSp6) and the excess alumina series (FeSp8) (Appendix Table 2), allowing for an independent check that reducing experimental conditions were achieved. Measured Fe_{VI}^{+3}/Fe^{tot} are very low for all samples measured (Appendix Table 2). Neglecting FeSp6_2, Fe_{VI}^{+3}/Fe^{tot} varies between 0.1 and 0.03 for the FeSp6 series. FeSp6_2 is the lowest

Fe# sample measured by Mössbauer, and therefore, the most difficult to precisely measure. This range of Fe_{VI}^{+3}/Fe^{tot} is similar to that determined for spinels synthesized via flux crystallization between IW+1.6 and IW-0.3 (Fe_{VI}^{+3}/Fe^{tot} = 0.03-0.14, Halenius et al., 2002). Thus, the reduced nature of the spinels synthesized in the FeSp6 series provide a more direct analog to remotely sensed lunar spinels.

The Fe^{+3} contents of spinels from the FeSp8 series are less well constrained. For example, FeSp8_1 Fe_{VI}^{+3}/Fe^{tot} is 0.17, whereas, for FeSp8_2 Fe_{VI}^{+3}/Fe^{tot} is 0.03. FeSp8_3 and FeSp8_4 could not be successfully fit with the same routine applied to the remainder of the samples, leaving their Fe_{VI}^{+3}/Fe^{tot} uncertain (Appendix Table 2). Mössbauer spectra are given in Appendix Table 3.

V-NIR spectra

Effect of iron. Increasing Fe content in (Fe,Mg) aluminate spinel increases the abundance of all Fe cation species (Fe_{IV}^{+2}, Fe_{VI}^{+2}, Fe_{VI}^{+3}). Thus, it is expected that spinel becomes a uniformly stronger absorber across the V-NIR with increasing Fe content. The individual V-NIR spectra of the FeSp6 series, in which samples increase systematically in Fe#, are shown in Figure 2.

Several notable features are present in the V-NIR spectra. First, the long wavelength bands (>2000 nm) are present even at extremely low Fe content. FeSp6_1 and FeSp6 _2 both have <1 Fe# and yet possess prominent bands centered near 2000 and 2800 nm. The strength of these bands has been noted previously, and they are associated with crystal field electronic transitions of Fe_{IV}^{+2} (e.g. Slack, 1964; Gaffney, 1973; Mao and Bell, 1975; Halenius et al., 2002; Skogby et al. 2003). These longer wavelength bands begin to saturate at relatively moderate Fe

content (>5 Fe#). This phenomenon can be observed by plotting the ln(reflectance$_{min}$) parameter, which is inversely related to band strength, of the 2000 and 2800 nm bands against Fe# (Figure 3). For >15 Fe#, ln(reflectance$_{min}$) at 2000 and 2800 nm reaches a minimum value and does not change with increasing Fe content.

Second, spinels with <6 Fe# do not display prominent shorter wavelength bands (<1000 nm), and therefore share spectral properties similar with Group 1 spinel identified in basin walls and large craters on the Moon (e.g. Pieters et al., 2014). However, other variables that may affect <1000 nm band strengths, such as cooling rate and sample texture, must be considered before spinel compositions can be reasonably estimated based on spectral properties. These additional considerations are discussed in more detail in following sections.

Third, spinels with >6 Fe# display two well-defined bands centered near 700 and 1000 nm and are more spectrally similar to the Group 2 spinels associated with pyroclastic deposits discussed by Yamamoto et al. (2013). Collectively, these bands are referred to as the "1000 nm bands" here. The strength of these bands progressively increase with increasing Fe# (Figure 2), and do not saturate, as did the longer wavelength bands, even for the most Fe-rich composition explored (Figure 3).

Across the range of Fe contents explored, ln(reflectance$_{min}$) for the band at 1000 nm is linearly correlated with $[Fe_{VI}^{+2}]_{apfu}$ (apfu = atoms per functional unit, Figure 3a), with a reflectance coefficient of 9.04±1.50 $[Fe_{VI}^{+2}]^{-1}{}_{apfu}$ (95% confidence, R^2=0.90). Note that ln(reflectance$_{min}$) can only be calculated for spectra that have an observable absorption band near 1000 nm – for those samples without 1000 nm bands (FeSp6_1 – FeSp6_4), the minimum reflectance value is calculated by simply averaging the reflectance between 825 and 1100 nm. At 2000 nm, samples with >0.05 $[Fe_{IV}^{+2}]_{apfu}$ show signs of saturation (Figures 2 and 3b).

However, at low Fe# there is a linear relationship between ln(reflectance$_{min}$) and $[Fe_{IV}^{+2}]_{apfu}$. Using samples FeSp6_1-4, the reflectance coefficient for the 2000 nm band is 35.50 ± 6.81 $[Fe_{IV}^{+2}]^{-1}_{apfu}$ (95% confidence, R^2=0.95). Similar to the 2000 nm band, samples with >0.05 $[Fe_{IV}^{+2}]_{apfu}$ show signs of saturation at 2800 nm (Figures 2 and 3c) . Although there a general negative relationship between ln(reflectance$_{min}$) and $[Fe_{IV}^{+2}]_{apfu}$ for the lowest Fe# samples at 2800 nm, we choose to not report a reflectance coefficient as unsatisfactory fits are achieved for a regression forced through the origin. This may reflect a small contribution of OH to longer wavelength region of the V-NIR. Concentrations of Fe species are calculated for Q = 0.82 ($Q = X_{VI}^{B} - X_{IV}^{B}$ AB_2O_4 spinel, where the A and B cations are not restricted to their ordered site), as supported by the Mössbauer spectra and cooling rate-ordering model (discussed below), and assume all Fe is Fe^{+2}.

Effect of particle size. In addition to Fe abundance, band strength in the V-NIR is also dependent on the mean free path length of light travelling through a mineral lattice. Consequently, coarser particles are expected to be uniformly better absorbers, keeping all other variables constant. To demonstrate the magnitude of this effect in the synthetic spinels produced for this study, spectra of additional particle size separates were acquired for select samples from the FeSp6 series. A comparison of the different particle size separates (<45 μm, 45-75 μm, 75-125 μm) is shown in Figure 4. From Figure 4, it is apparent that both the 1000 nm and the >2000 nm bands increase in strength with increasing particle size, as expected. The increase in band strength is more pronounced at the longer wavelengths than for the 1000 nm bands. In general, the effect of varying particle size on band strength of these synthetic samples is small compared to the effect of increasing Fe#. It has been shown that <45 μm particle size fraction dominates the optical properties of the lunar soils at V-NIR wavelengths (Pieters et al., 1993;

414 Fischer 1995). Consequently, the <45 μm particle size separates of the spinels synthesized here
415 provide the most direct analogy to lunar spinels and are the focus of the work presented here.
416
417 **Mid-IR spectra**
418 Full resolution laboratory emissivity (calculated as 1 – reflectace, Kirchoff's Law)
419 spectra for the FeSp6 series are plotted across the mid-IR spectral range (1250 – 400 cm^{-1} or
420 8000 – 25000 nm) in Figure 5. Diagnostic spectral features include the primary Christiansen
421 feature (CF) observed near ~980 cm^{-1} (~10200 nm) and the secondary CF observed near ~620
422 cm^{-1} (~16100 nm). Mid-IR laboratory spectra show a systematic shift of the primary and
423 secondary CF positions to lower wavenumbers (longer wavelengths) as the Fe# increases. While
424 the 18.9 Fe# sample (FeSp6_9) falls off the trend, it is clear in Figure 6, the primary and
425 secondary CF position is related to Fe# for the other FeSp6 series compositions. FeSp6_9 is not
426 used for regression purposes. Thus, the primary and secondary CF positions can be used to
427 distinguish between compositions of aluminate spinel. The equations fit to the CF positions
428 (wavenumber, cm^{-1}) are as follows:

$$CF1_{pos.} = -0.460 \pm 0.035 \cdot Fe\# + 982.972 \pm 0.526, R^2 = 0.99$$

$$CF2_{pos.} = -0.705 \pm 0.175 \cdot Fe\#^{0.5} + 625.667 \pm 0.559, R^2 = 0.93$$

429 A similar linear trend is observed between the primary and secondary CF positions and Fe# in
430 emissivity spectra of the olivine solid solution series (Hamilton, 2010). Diagnostic absorptions
431 in the reststrahlen band (RB) regions were identified near ~865, 755, 706, and 530 cm^{-1} (~11600,
432 13200, 14200, and 18900 nm). As seen in Figure 6, the RB bands near ~865 and 530 cm^{-1} also
433 have linear relationships with Fe# as the diagnostic band positions shift to lower wavenumbers
434 (longer wavelengths). The equations fit to the RB positions (wavenumber, cm^{-1}) are as follows:

$$RB1_{pos.} = -0.280 \pm 0.083 \cdot Fe\# + 866.643 \pm 1.236, R^2 = 0.90$$

$$RB4_{pos.} = -0.208 \pm 0.065 \cdot Fe\# + 532.828 \pm 0.960, R^2 = 0.89$$

Thus, diagnostic absorption bands in the RB regions can also be used to distinguish between aluminate spinel compositions. Similar trends are observed between RB absorption band positions and Fe# in spinels (Cloutis et al., 2004) and olivines (Hamilton, 2010). Uncertainties in regression equations are 95% confidence intervals.

DISCUSSION

Distribution of Fe species in spinel

Experimental and theoretical arguments suggest the strength of 1000 nm bands in spinel are potentially sensitive to Fe_{VI}^{+2} and Fe_{VI}^{+3} content (e.g. Dickson and Smith, 1976; Halenius et al., 2002; Mao and Bell, 1975; Taran et al., 2005). Both Fe_{VI}^{+2} and Fe_{VI}^{+3} will increase with Fe#, but other variables, such as fO_2, cooling rate, and aAl$_2$O$_3$/(aMgO+aFeO) (where a denotes the activity of an oxide) can affect the distribution of Fe species within the spinel lattice. As such, these variables should affect the relative concentrations of different Fe species for a given bulk Fe content, and consequently, their importance must be evaluated when linking spectral characteristics to mineral composition. The following discussion is focused on determining the root causes of 1000 nm bands in aluminate spinel and the relative strength of the 1000 and 2000 nm bands. This information is then applied to providing further geologic context to Group 1 and 2 spinel identifications on the lunar surface.

Effect of aAl$_2$O$_3$ on V-NIR spectra

Aluminate spinel can accommodate significant non-stoichiometry. This non-stoichiometry affects the point defect population, and potentially, the distribution of Fe ions in the spinel lattice. Thus, $a\mathrm{Al_2O_3}$ may be expected to affect the V-NIR spectral properties of aluminate spinel, which are dependent on the particular coordination environments of the absorbing species. We stress that the potential effect of Al-rich non-stoichiometry is large and increases rapidly with temperature. For example, at 1 GPa pure Mg-aluminate spinel is capable of hosting ~2.04 Al per 4 O at 1400 °C and ~2.14 Al per 4 O at 1600 °C (Watson and Price, 2002). There is some uncertainty regarding how excess $\mathrm{Al_2O_3}$ can be accommodated into the spinel structure, but three potential mechanisms (defect disorders) are argued as reasonable (Murphy et al., 2010); the extrinsic reactions are:

$$3Al_2O_3 + 2Mg_{IV}^{x} = 2Al_{IV} + O_i^{''} + 2MgAl_2O_4 \text{ , (1)}$$

$$4Al_2O_3 + 3Mg_{IV}^{x} = 2Al_{IV} + V_{IV}^{''} + 3MgAl_2O_4 \text{, and (2)}$$

$$4Al_2O_3 + 3Mg_{IV}^{x} + Al_{VI}^{x} = 3Al_{IV} + V_{VI}^{'''} + 3MgAl_2O_4 \text{. (3)}$$

Reactions (1)–(3) are written in Kröger-Vink notation (e.g. Schmalzried, 1981, pp 39): subscripts refer to lattice sites and superscripts refer to charge on that site relative to whatever species occupies the site in the perfect crystal. A subscript of "*i*" indicates a interstitial site, i.e., an interstice not occupied in the perfect crystal. For superscripts, a prime is a single negative charge, a dot is a single positive charge, and an "×" indicates neutrality. Thus, Al_{IV} is an "antisite" defect, i.e., an Al^{+3} occupying a tetrahedral site that, in the perfect, non-disordered spinel crystal holds an Mg^{+2}; $O_i^{''}$is an interstitial O^{-2}; $V_{VI}^{'''}$ is a vacant octahedral site, one that normally would have contained an Al^{+3} (i.e., Al_{IV}^{X}) in the perfect crystal. (An important aspect of

point-defect reactions such as these is that matter, charge, and lattice sites must all be conserved, which is the case for each of these reactions.) Note that all these reactions create the Al antisite defect when excess Al_2O_3 is incorporated into the spinel structure. Consequently, in spinel where $a Al_2O_3/(a FeO + a MgO)$ is high (i.e. spinel with excess Al_2O_3), reactions (1, 2, and 3) are driven toward products and Al_{IV} is produced.

Under typical geologic conditions, Mg and Fe^{+2} favor the tetrahedral site (generically the A site, in AB_2O_4) in aluminate spinel, and it is Fe_{IV}^{+2} that causes the prominent 2000 nm absorption that is common to all remotely sensed lunar spinels. Bands near 1000 nm in spinel are associated, in part, with Fe^{+2} partitioning onto the octahedral site that is normally occupied by Al^{+3} or Cr^{+3} as denoted in the following disorder reaction (Navrotsky and Kleppa, 1967):

$$Fe_{IV}^{X} + Al_{VI}^{X} = Fe_{VI}^{'} + Al_{IV} \quad (4)$$

Following reaction (4), there are two ways to generate Fe_{VI}^{+2}, where Fe_{VI}^{+2} is equivalent to $Fe_{VI}^{'}$ and Fe_{IV}^{+2} is equivalent to Fe_{IV}^{x}. First, increasing bulk Fe^{+2} content in spinel creates Fe_{VI}^{+2} and Fe_{IV}^{+2} in order to maintain equilibrium in reaction (4). Second, increasing the degree of disorder (reaction (4) driven to the right) generates Fe_{VI}^{+2} at the expense of Fe_{IV}^{+2}, causing $Fe_{IV}^{+2}/Fe_{VI}^{+2}$ to decrease.

In order to maintain the equilibrium described by reaction (4), the generation of Al_{IV} through reactions (1, 2, and 3) reduces $[Fe_{VI}^{+2}]$ for a given total Fe content, increasing $Fe_{IV}^{+2}/Fe_{VI}^{+2}$. In turn, lowering $[Fe_{VI}^{+2}]$ should result in weaker 1000 nm bands, assuming Fe_{VI}^{+2} contributes to these features. In fact, this is what is observed in our experimental dataset.

Figure 7 compares the V-NIR spectra of aluminate spinels that are nominally stoichiometric and aluminate spinels that contain excess Al_2O_3 (non-stoichiometric, Al-rich) but have the same Fe#. The samples with excess Al_2O_3 (dashed and dotted lines, FeSp8 series, Figure 7) have significantly weakened 700 and 1000 nm bands, whereas their 2000 and 2800 nm bands are strengthened compared to the nominally stoichiometric spinel (FeSp6 series, solid lines). These observations provide experimental support for the coupling of reactions (1, 2 and 3) with reaction (4) and strongly implies that $[Fe_{VI}^{+2}]$ is a major control on the strength 1000 nm bands in aluminate spinel. Moreover, these observations confirm $[Fe_{IV}^{+2}]$ as the major control on 2000 and 2800 nm band strength.

It is important to stress that lunar spinels are close to stoichiometric, even in systems that have a high normative abundance of plagioclase. This is because 1) $a$$Al_2O_3$/($a$FeO+$a$MgO) of melts with high normative plagioclase and saturated in spinel is still close to one (calculated using MELTS software, Ghiorso and Sack, 1995). Only values of $a$$Al_2O_3$/($a$FeO+$a$MgO) >>1 generate spinel with significant excess Al_2O_3, and 2) the maximum degree of non-stoichiometry for spinel below 1000°C is very small (Watson and Price, 2002). Lunar spinels excavated from mid to lower crustal depths likely had significant time to reequilibrate at temperatures where only minor amounts of excess Al_2O_3 could be accommodated. Indeed, the composition of Mg-rich aluminate spinels found in lunar troctolities are very nearly stoichiometric (e.g. Prinz et al. 1974, Ridley et al., 1973). Thus, the synthesis runs that are nominally stoichiometric are most applicable to lunar conditions (FeSp6 series). The FeSp8 series demonstrates the coupling of reactions (1, 2, and 3) with reaction (4) and highlights the importance of $[Fe_{VI}^{+2}]$ in generating the 1000 nm bands in spinel.

524 **Effect of cooling rate on V-NIR spectra**

525 The ratio of Fe_{IV}^{+2} to Fe_{VI}^{+2} in aluminate spinel can be quantified using the ordering
526 parameter, Q ($Q = X_{VI}^{B} - X_{IV}^{B}$ for AB_2O_4 spinel, where the A and B cations are not restricted to
527 their ordered site). The equilibrium for reaction (4) is highly temperature sensitive, where
528 increasing temperature favors higher entropy states, and consequently lower Q values and lower
529 $Fe_{IV}^{+2}/\,Fe_{VI}^{+2}$ (reaction (4) driven to the right). Similarly, at absolute zero, Q goes to unity and no
530 $Fe_{VI}^{+2}$is present in stoichiometric (Mg,Fe) aluminate spinel.

531 Disordering in reaction (4) is a thermally activated process, hindering the approach to an
532 equilibrium distribution at low temperatures and fast cooling rates (Dodson, 1973).
533 Experimental evidence supports rapid attainment of equilibrium ordering at moderate (>500°C)
534 temperatures for most geologic cooling rates, but at lower temperatures ordering kinetics become
535 sluggish and higher degrees of disorder become locked in upon cooling. Given that $Fe_{IV}^{+2}/Fe_{VI}^{+2}$
536 strongly controls the relative strengths of the 1000 and 2000 nm bands (Figure 7), it is expected
537 that the relative strength of the 1000 and 2000 nm bands is sensitive to the cooling rate of a
538 particular spinel.

539 To quantify the sensitivity of Fe^{+2}-Al ordering to cooling rate we solved the rate law
540 equation for different cooling rates (Salje, 1988):

541 $$\frac{dQ}{dt} = \frac{\gamma \exp(-\frac{\Delta H}{RT})}{2RT} \frac{\delta \Delta G}{\delta Q} \quad (5)$$

542 and

543 $$\Delta G = -Q + \frac{1}{2}a'(T - T_c)Q^2 + \frac{1}{6}c'Q^6 \text{ , } (6)$$

544

where a' and c' are fitting parameters for a Taylor expansion of the Gibbs free energy potential, T_c is a critical temperature, γ is the frequency factor, and ΔH is the activation energy. We use the ΔH, γ, T_c, and c' fit for a stoichiometric hercynite (Harrison et al., 1998) and adopt an $a' = 0.002$ while ranging cooling rate from (10^3 to 10^{-13} °C s^{-1} or $3x10^{15}$ to 3 °C Ma^{-1}). Examples of solutions for a range of cooling rates are plotted in Figure 8a. At low temperature, Q deviates from the equilibrium Fe_{IV}^{+2}-Fe_{VI}^{+2}distribution (O'Neill and Navrotsky, 1983, dashed line, Figure 8) and closes (stagnates) at a value that is inversely proportional to cooling rate. The value of Q at closure is plotted as a function of cooling rate in Figure 8b.

Values of Q can be calculated for the synthetic spinels produced here from the distribution of Fe coordination states as determined by Mössbauer spectroscopy. This calculation requires the assumption that Fe^{+2} and Mg are equally disordered for a given sample. Studies comparing Q for spinel *ss* and hercynite have demonstrated that both minerals share similar Q-temperature relationships (e.g. Redfern et al. 1998), supporting this assumption. Given a cooling rate of 10^{-2} °C s^{-1} for the laboratory spinels, the cooling model predicts a Q value of 0.82. Calculations of Q from Mössbauer spectra range between 0.65 and 0.93, with an average of 0.80±0.17 (95% confidence) for the FeSp6 series. This is in good agreement with the modeled value and provides confidence in applying the cooling model to natural scenarios (see below). Mössbauer spectra were not used to quantify cation ordering in the FeSp8 series because the fitting routine did not converge for all samples in this series.

A single drop-quench cooling experiment was conducted to directly explore the effect of cooling rate on aluminate spinel V-NIR spectra (FeSp10 series). The drop-quench spinel had a 31% lower ln($reflectance_{min}$) value at 1000 nm (greater band strength) compared to the more slowly cooled equivalent (FeSp6_11, calculated using scaled spectra). For cooling rates of 100

and 1000 °C s^{-1}, the cooling rate-ordering model (Figure 8) predicts ln(reflectance$_{min}$) at 1000 nm to decrease by 55 and 75%, respectively, assuming ln(reflectance$_{min}$) at 1000 nm is inversely proportional $[Fe_{VI}^{+2}]$ and that $Q = 0.82$ for all samples of the FeSp6 series. Thus, the drop-quench experiment supports cooling rate and Fe_{VI}^{+2} being important controls of V-NIR spinel spectra, albeit with some discrepancy between the experimental observation and model prediction.

Spinel anorthosite and DMD spinel (Groups 1 and 2) – Relation to cooling rate

Given the sensitivity of aluminate spinel spectra to cooling rate, potential cooling scenarios must be evaluated for Group 1 and 2 spinels. The paleo-temperature field of the lunar mantle is not well known, but recent modeling of lunar thermal history suggests a radially averaged temperature of ~500 °C at 3.9 Ga for the lower crust (Zhang et al., 2013, preferred model: H50E100MR2500). This temperature is greater than the Fe^{+2}-Al ordering closure temperature associated with slowly cooled rocks (closure temperature <400 °C for cooling rates $<10^{-13}$ °C s^{-1}, McCallum and O'Brien, 1996). Moreover, the generation of spinel anorthosite implies additional magmatic heat input into the crust local to the spinel anorthosite lithologies, raising the temperature above the radial average. Thus, if spinel anorthosite (Group 1) was excavated from the mid to lower lunar crust, as implied by its association with basin walls and large craters, this suggests that the spinels were in a relatively disordered state before excavation. Similarly, DMD spinels associated with pyroclastic eruptions (Group 2) are expected to rapidly cool from magmatic to ambient temperatures. Consequently, the Fe^{+2}-Al closure for both Group 1 and 2 is likely set by the relatively rapid cooling at or near the lunar surface, and as such, near-surface cooling rates need to be evaluated.

590 Saal et al. (2008) argued for cooling rates of 2-3 °C s^{-1} for lunar pyroclasitc glass beads
591 on the basis of measured volatile loss profiles. This rate is supported by textural comparisons
592 betweeen experimental and natural lunar pyroclastic glass beads (Arndt et al., 1987) and has
593 been interpreted to require an insulating vapor cloud. We use this rate as a lower limit for the
594 Group 2 spinels. However, the high temperature cooling rates of pyroclastic deposits are
595 expected to be faster if cooled under vacuum (~1000 °C s^{-1} at ~1000 °C, Arndt et al., 1979). We
596 take 1000 °C s^{-1} as an upper limit for Group 2 cooling rates.

597 Cooling rates for spinels found in basin walls and large craters (Group 1) are more
598 difficult to estimate, but limits can be evaluated. Erosion of outcropping rock on the Moon is
599 slow, with estimates for the combined effects of mass wasting and spallation totaling to 1 cm
600 Ma^{-1} or ~45 m over lunar history (Arvidson et al., 1975), suggesting the spinel-bearing materials
601 observed on the Moon are sourced from the upper 10s of meters of the material exposed during
602 impact related excavation. Studies of mare basalts infer cooling rates on the order of 10^{-4} °C s^{-1}
603 near 500°C for flows that are on the order of meters in thickness (Takeda et al., 1975). This rate
604 would apply to exposed material where typical amounts of erosion have occurred. If erosion
605 rates were extraordinarily high, the spinel anorthosite material exposed today could have been
606 sourced from deeper, better-insulated rocks. Cooling rates for lunar rocks inferred to be sourced
607 from ~200 m deep are 10^{-9} °C s^{-1} (McCallum and O'Brien, 1996), which is a reasonable lower
608 limit on the cooling rate for the spinels exposed on surface of the Moon via excavation from mid
609 to lower lunar crust.

610 The effect of these cooling rates on spinel order-disorder can be evaluated using the
611 calculations presented in Figure 8b. Compared to the laboratory cooling rate near 500°C (~10^{-2}
612 °C s^{-1}), a cooling rate of 10^{-9} °C s^{-1} results in an increase of 0.08 for Q, or a 44% decrease in

613 $[Fe_{VI}^{+2}]$. For the alternative scenario involving shallower sourced material for the spinel
614 anorthosite, a cooling rate of 10^{-4} °C s^{-1} results in an increase of 0.03 for Q, or a 17% decrease in
615 $[Fe_{VI}^{+2}]$. The DMD spinels (Group 2) likely cooled more rapidly than the laboratory spinels, and
616 correspondingly, the 1000 nm bands should be relatively strong. For the slow cooling
617 pyroclastic scenario (Saal et al, 2008), a cooling rate of 1 °C s^{-1} results in a decrease of 0.04 for
618 Q, or a 22% increase in $[Fe_{VI}^{+2}]$. For pyroclastic material cooling into vacuum, a cooling rate
619 1000 °C s^{-1} results in a decrease of 0.1 for Q, or a 75% increase in $[Fe_{VI}^{+2}]$.
620

621 ## IMPLICATIONS

622 ### Mid-IR

623 Analysis of the lunar spinel locations identified by V-NIR techniques (e.g., Pieters et al.,
624 2014) across the mid-IR spectral range is limited by the spectral resolution and spectral coverage
625 of current sensors. Our results indicate that the mid-IR spectral range can be used to distinguish
626 aluminate spinel compositions from: (1) one another based on the position of diagnostic spectral
627 features such as the CF and RB and (2) other silicate minerals found on the lunar surface such as
628 plagioclase, pyroxene, and olivine. As seen in Figure 6, diagnostic spectral features of aluminate
629 spinel systematically shift to lower wavenumbers (longer wavelengths) as the Fe# increases. In
630 addition, the CF and RB positions of aluminate spinel occur at lower wavenumbers (longer
631 wavelengths) that are distinct from the CF and RB positions of other silicate minerals like
632 plagioclase, pyroxene, and olivine. Detailed coordinated analyses of remote observations of lunar
633 spinel locations identified by V-NIR (e.g., Pieters et al., 2014) using additional hyperspectral
634 mid-IR data sets, along with the laboratory mid-IR spectra of aluminate spinels presented here,
635 may be able to constrain the abundances of spinel and plagioclase in spinel-rich areas

636

637 **Spinel anorthosite (Group 1)**

638 The Group 1 spinels associated with spinel anorthosite lack observable 1000 nm bands
639 (e.g. Pieters et al., 2014). The results of the current work have demonstrated the effects of
640 particle size, cooling rate, and Fe content on 1000 nm band strengths for spinels at lunar-relevant
641 fO_2. Making assumptions for particle size and cooling rate of the Group 1 spinels, we can
642 estimate the composition of the spinels that are most consistent with the remotely observed
643 spectral characteristics. First, we have assumed that the particle sizes of the synthetic spinel
644 studies here (<45 um) is an appropriate analog for the textures of lunar spinels (Pieters et al.,
645 1993; Fischer 1995). As discussed in the cooling rate section, the cooling rate for Group 1
646 spinels is uncertain, but different scenarios can be evaluated. Essentially, slower cooling rates
647 are associated with deeper burial and weaker 1000 nm bands for a given Fe content. Compared
648 to the laboratory cooling rates (~10^{-2} °C s^{-1}), the slowest cooling scenario results in ~50% less
649 Fe_{VI}^{+2}. The lowest Fe# spinel that has prominent 1000 nm bands is FeSp6_6 (Fe# = 6.2,
650 Fe_{VI}^{+3}/Fe^{tot}= 0.06). Accounting for cooling rate, this implies that spectra of lunar spinels with
651 >12 Fe# (<88 Mg#) would have observable 1000 nm bands. Generation of spinel with <12 Fe#
652 suggests Group 1 formation occurred within a relatively Fe-poor system, such as those associated
653 with Mg-Suite magmatism (Prissel et al. 2014).

654 It is also possible to form aluminate spinel in more Fe-rich systems, possibly associated
655 with mare basalt liquids or picritic liquids (Gross and Treiman, 2011), but experiments have
656 shown that lowest Fe# picritic glass composition would produce spinel with 20 Fe# when reacted
657 with anorthite (A15C, Prissel et al., 2014). A cooling rate of 10^{-19} °C s^{-1}, which corresponds to Q
658 at closure equal to 0.946, is sufficient to raise the threshold for observable 1000 nm bands to 20

659 Fe#. This cooling rate is much slower than rates calculated for lunar highlands samples inferred
660 to be very deeply buried (6×10^{-13} °C s^{-1}, 21 km depth, McCallum and O'Brien, 1996) and would
661 result in negligible cooling over the course of lunar history. This calculation assumes a Q value
662 of 0.82 for the FeSp6 series, as supported by the cooling rate of these samples and the Mössbauer
663 spectra. Thus, the petrogenesis of Group 1 spinels most plausibly involved Mg-Suite magmas,
664 implying a global distribution of Mg-suite magmatism. This association is supported by the link
665 between Group 1 and deep crustal lithologies (Pieters et al., 2014) and the low Cr# of Group 1
666 spinels (e.g. Cloutis et al., 2004), as the Mg-Suite is also associated with deep crustal lithologies
667 and is relatively Cr-poor rock suite (e.g. Elardo et al., 2011). However, it is important to stress
668 that further reduction of Fe, space weathering, and mixing with plagioclase could all act to
669 weaken the 1000 nm bands independently of Fe# of the spinel (e.g. Cheek and Pieters, 2014;
670 Isaacson et al., 2014). Moreover, chromite spinels are more ordered for a given cooling rate due
671 to the strong ordering of Cr^{+3} onto the octahedral site (e.g. Navrotsky and Kleppa, 1967), and
672 consequently, a small (undetectable) amount of Cr may also cause an underestimate of Fe# based
673 on the above analysis.
674
675 **DMD spinel at Sinus Aestuum (Group 2)**
676 The spinels observed in the DMD of Sinus Aestuum are unique for the Moon and display
677 both short and long wavelength bands across the V-NIR (Yamamoto et al, 2013). The relative
678 strength of the short and long wavelength bands in aluminate spinel is an expression of
679 $Fe_{VI}^{+2}/Fe_{IV}^{+2}$, and thus, cooling rate. To quantify the relative strength of the 1000 and 2000 nm
680 bands of the FeSp6 series spinels, we calculated the product of the reflectance coefficient for the
681 1000 and 2000 nm bands (Figure 3) and abundance of Fe_{VI}^{+2} and Fe_{IV}^{+2}, respectively. The ratio of

these two products defines the relative strengths of the 1000 and 2000 nm bands independently of Fe#. This ratio is 0.0357 ± 0.0090 (95% confidence) for the FeSp6 series. The ratio of ln(reflectance$_{min}$) values for 1000 and 2000 nm bands has also been calculated for continuum-corrected spectra reported by Yamomato et al. (2013), yielding values of 0.108, 0.114, 0.115, and 0.103 for four of their reported spectra (A7, B14, C2, and F4). The average of this population is 0.109 ± 0.0109 (95% confidence). The higher band minimum ratio (stronger 1000 nm relative to 2000 nm bands) measured at Sinus Aestuum compared to the synthetic spinels are consistent with a relatively fast cooling rate of Group 2 spinels compared to the spinels synthesized for this study.

Fast cooling rates for Sinus Aestuum spinels are consistent with a pyroclastic origin (cooling in the presence or absence of a vapor cloud). Arndt et al. (1987) calculate cooling rates of 1080 and 86 °C s^{-1} across 1050 °C under vacuum for orange glass bead sizes of 0.16 mm and 2.0 mm, respectively. The presence a vapor cloud is expected to slow cooling rates. The cooling rate-ordering model (Figure 8) predicts a cooling rate of 1000 °C s^{-1} results in a 102% increase in the 1000 nm and 2000 nm ln(reflectance$_{min}$) ratio band compared to cooling at 10^{-2} °C s^{-1}. The difference between the 1000 nm-2000 nm ln(reflectance$_{min}$) ratio associated with Sinus Aestuum and the FeSp6 series is large, a 207 ± 56 % increase. Thus, the large offset between Sinus Aestuum and FeSp6 1000 nm-2000 nm ln(reflectance$_{min}$) ratios is more consistent with cooling in the absence of a vapor cloud and small grain size, but may also may partly reflect relatively small pyroclastic bead size, high [Fe_{VI}^{+3}], systematic errors introduced during continuum or thermal corrections of the Sinus Aestuum spectra.

Further, it is important to note that the V-NIR spectra of the Group 2 spinels do not necessarily require a higher Fe# compared to the Group 1 spinels, as faster cooling, and

potentially higher [Fe_{VI}^{+3}], should act to preferentially strengthen 1000 nm bands. However, the age inferred from superposition relations and the density of craters at Sinus Aestuum (Yamamoto et al., 2013) argues against a relationship to early Mg-suite magmatism and supports a relationship to later, more Fe-rich magmas.

Figure Captions:

Figure 1, Backscattered electron image of typical run products: Image a) FeSp6_7 (10.2 Fe#), and image b) FeSp6_6 (6.2 Fe#). No obvious gradients in contrast are present in either image, indicating a homogenous distribution of Mg and Fe. Large (~100 μm diameter) and small scale (~1 μm diameter) porosity is present in all samples. The small scale porosity is more easily observed in the FeSp6_6 sample (b). Small modes of ferro-periclase were observed during inspection of some samples using back-scatter electron imaging (a).

Figure 2, V-NIR spectra from the FeSp6 series (<45 μm) a) scaled and b) unscaled. The lowest Fe# samples only display bands at 2000 and 2800 nm. The lowest Fe# with observable 700 and 1000 nm bands is FeSp6_7 (6.2 Fe#). Above 6.2 Fe# all spinels display four prominent band centers at 700, 1000, 2000, and 2800 nm are present. The 1000 nm band is uniformly stronger than the 700 nm band.

Figure 3, Correlations between ln(reflectance$_{min}$) and various Fe species for the a) 1000, b) 2000, and c) 2800 nm bands. a) ln(reflectance$_{min}$) for the 1000 nm band correlates linearly with [Fe_{VI}^{+2}]$_{apfu}$, or equivalently, Fe#. b) At low Fe contents (FeSp6_1-4) there is a linear relationship

between ln(reflectance$_{min}$) for the 2000 nm band $[Fe_{IV}^{+2}]_{apfu}$. c) Similar to the 2000 nm band, high Fe samples with show signs of saturation at 2800 nm. There is a negative relationship between ln(reflectance$_{min}$) and $[Fe_{IV}^{+2}]_{apfu}$ for the lowest Fe# samples at 2800 nm, but the regression does not pass through the origin. This may reflect a small contribution of OH to longer wavelength region of the V-NIR. Concentrations of Fe species are calculated for Q = 0.82, as supported by the Mössbauer spectra and cooling rate-ordering model (see section V-NIR- Mössbauer - Cooling Rate), and assume all Fe is Fe^{+2}.

Figure 4, Scaled reflectance spectra for FeSp6 series illustrating the effect of particle size on FeSp6 V-NIR spectra: The solid lines are the <45 μm particle size spectra (scaled), and the dashed and dotted lines are the 45-75 and 75-125 μm particle size spectra, respectively. In all cases, increasing particle size results in stronger bands at 700, 1000, 2000, and 2800 nm, in line with the correlation between mean free path length and particle size.

Figure 5, Mid-IR spectra from the FeSp6 series (<45 μm). Spectra are offset for clarity and vertical lines highlight the positions of identified features. The primary Christiansen feature is near ~980 cm^{-1} (~10200 nm) and the secondary CF is near ~620 cm^{-1} (~16100 nm). Reststrahlen band regions are located near ~865, 755, 706, and 530 cm^{-1} (~11600, 13200, 14200, and 18900 nm). The mid-IR spectrum for FeSp6_9 (18.9 Fe#) is anomalous compared to the other mid-IR spectra of the FeSp6 series and is not used for further comparisons.

Figure 6, Mid-IR spectral systematics from the FeSp6 series (<45 μm). The positions of both Christiansen features (CF) are negatively related to Fe#. a) The primary CF position is linearly

751 related to Fe#, and b) the secondary CF position is linearly related to Fe#$^{0.5}$. Four Reststrahlen
752 bands (RB) are identified (Absorptions 1-4, c-f). The positions of Absorption 1 and Absorption
753 4 show clear, negative relationships to Fe#. The position of Absorption 2 is only weakly
754 correlated with Fe#, and consequently, no regression is reported for this band. The position of
755 Absorption 3 appears independent of Fe#.
756
757 Figure 7, Effect of excess Al_2O_3 on V-NIR spectra: Samples for the FeSp8 series were prepared
758 by mixing 7.5 wt% additional Al_2O_3 into the same oxide powders mixed for the FeSp6 series
759 (dashed lines). This ensures an excess of Al_2O_3 was present in the FeSp8 series spinels over their
760 baseline (FeSp6). Compared to the equivalent samples from the FeSp6 series (solid lines), the
761 samples with excess Al_2O_3 have severely weakened 700 and 1000 bands (dashed and dotted
762 lines). Moreover, the 2000 and 2800 nm bands are relatively strengthened. This result is
763 consistent with the coupling of reactions (1 and 2) with reaction (3), limiting the degree of
764 disordering of Fe in aluminate spinel. Less Al_2O_3 (2.5 wt %) was added to the dotted line sample
765 (panel c, FeSp8_4), and this spectrum is intermediate to the FeSp6 baseline and the sample with
766 more Al_2O_3 added. Note the presence of a new band located at 550 nm in the samples with
767 excess Al_2O_3.
768
769 Figure 8, Cooling Model: a) Examples of solutions for selected linear cooling rate scenarios and
770 b) Q at closure for various cooling rate scenarios. a) At temperatures >700 °C, Q follows an
771 equilibrium distribution for the selected range of cooling rates explored. At lower temperatures,
772 Q departs from the equilibrium value and eventually stops evolving after a given amount of
773 cooling. More rapid cooling results in lower Q (greater amounts of disorder) at closure. c)

774 Values of Q at closure have been tabulated for a wide range of cooling rates applicable to Group
775 1 and Group 2 spinel exposures. The relationship between Q and cooling rate is not linear.
776 Rather, Q asymptotically approaches 1 with progressively slower cooling rates.

777

778 References:

779

780 Adams, J.B. (1974) Visible and near-infrared diffuse reflectance spectra of pyroxenes as applied
781 to remote sensing of solid objects in the solar system. Journal of Geophysical Research,
782 79, 4829-4836.
783 Arndt, J., Flad, K., and Feth, M. (1979) Radiative cooling experiments on lunar glass analogues.
784 Lunar and Planetary Science Conference Proceedings, 10, p. 355-373.
785 Arndt, J., and Von Engelhardt, W. (1987) Formation of Apollo 17 orange and black glass beads.
786 Journal of Geophysical Research, 92, E372-E376.
787 Arvidson, R., Drozd, R.J., Hohenberg, C.M., Morgan, C.J., and Poupeau, G. (1975) Horizontal
788 transport of regolith, modification of features, and erosion rates on the lunar surface.
789 Moon, 13, 67-79.
790 Bhattacharya, S., Chauhan, P., and Ajai. (2012) Discovery of orthopyroxene-olivine-spinel
791 assemblage from the lunar nearside using Chandrayaan-1 Moon Mineralogy Mapper
792 data. Current Science, 103, 21-23.
793 Burns, R.G. (1970) Crystal field spectra and evidence of cation ordering in olivine minerals.
794 American Mineralogist, 55, 1608-1632.
795 Cheek, L.C., Pieters, C.M., Reflectance spectroscopy of plagioclase and mafic mineral mixtures:
796 Implications for characterizing lunar anorthosites remotely, Submitted to American
797 Mineralogist, lunar highlands special issue
798 Cintala, M.J., and Grieve, R.A.F. (1998) Scaling impact melting and crater dimensions:
799 Implications for the lunar cratering record. Meteoritics & Planetary Science, 33, 889-912.
800 Cloutis, E.A., Sunshine, J.M., and Morris, R.V. (2004) Spectral reflectance-compositional
801 properties of spinels and chromites: Implications for planetary remote sensing and
802 geothermometry. Meteoritics & Planetary Science, 39, 545-565
803 Conel, J. E. (1969) Infrared emissivities of silicates: Experimental results and a cloudy
804 atmospheric model of spectral emission from condensed particulate mediums. Journal of
805 Geophysical Research, 74, 1614-1634.
806 Delano, J. (1990) Experimental constraints on the oxidation state of the lunar mantle. Lunar and
807 Planetary Institute Science Conference Abstracts, 21, p. 278.
808 Dhingra, D., and Pieters, C. (2011) Mg-Spinel Rich Lithology at Crater Copernicus. LEAG
809 Conference (2011).
810 Dhingra, D., Pieters, C.M., Boardman, J.W., Head, J.W., Isaacson, P.J., and Taylor, L.A. (2011)
811 Compositional diversity at Theophilus Crater: Understanding the geological context of
812 Mg-spinel bearing central peaks. Geophysical Research Letters, 38, L11209.

Dickson, B., and Smith, G. (1976) Low Temperature Optical Absorption and Mossbauer Spectra of Staurolite and Spinel. Canadian Mineralogist, 14, 206-215.

Dodson, M.H. (1973) Closure temperature in cooling geochronological and petrological systems. Contributions to Mineralogy and Petrology, 40, 259-274.

Donaldson Hanna, K. L., I. R. Thomas, N. E. Bowles, B. T. Greenhagen, C. M. Pieters, J. F. Mustard, C. R. M. Jackson, and M. B. Wyatt (2012) Laboratory emissivity measurements of the plagioclase solid solution series under varying environmental conditions, JGR, 117, E11,

Dyar, M.D., McGuire, A.V., and Ziegler, R.D. (1989) Redox equilibria and crystal chemistry of coexisting minerals from spinel lherzolite mantle xenoliths. American Mineralogist, 74, 969-980.

Elardo, S.M., Draper, D.S., and Shearer Jr, C.K. (2011) Lunar Magma Ocean crystallization revisited: Bulk composition, early cumulate mineralogy, and the source regions of the highlands Mg-suite. Geochimica et Cosmochimica Acta, 75, 3024-3045.

Fischer, E. M. (1995) Quantitative compositional analysis of the lunar surface from reflectance spectroscopy: Iron, aluminum, and a model for removing the optical effects of space weathering. Ph.D. dissertation, Brown University, Providence, RI.

Fogel, R.A., and Rutherford, M.J. (1995) Magmatic volatiles in primitive lunar glasses: I. FTIR and EPMA analyses of Apollo 15 green and yellow glasses and revision of the volatile-assisted fire-fountain theory. Geochimica et Cosmochimica Acta, 59, 201-215.

Gaffney, E.S. (1973) Spectra of tetrahedral Fe^{+2} $MgAl_2O_4$. Physical Review B, 8. 3484-3486.

Ghiorso, M.S., and Sack, R.O. (1995) Chemical mass transfer in magmatic processes IV. A revised and internally consistent thermodynamic model for the interpolation of extrapolation of liquid-solid equilibria in magmatic systems at elevated temperatures and pressures. Contributions to Mineralogy and Petrology, 119, 197-212.

Gross, J., and Treiman, A.H. (2011) Unique spinel-rich lithology in lunar meteorite ALHA 81005: Origin and possible connection to M-3 observations of the farside highlands. Journal of Geophysical Research-Planets, 116, E10009.

Hamilton, V. E. (2010) Thermal infrared (vibrational) spectroscopy of Mg-Fe olivines: A review and applications to determining the composition of planetary surfaces. Chemie der Erde, 70, 7-33

Hapke, B. (1993) Theory of Reflectance and Emittance Spectroscopy, Cambridge University Press, New York.

Harrison, R.J., Redfern, S.A.T., and O'Neill, H.S.C. (1998) The temperature dependence of the cation distribution in synthetic hercynite ($FeAl_2O_4$) from in-situ neutron structure refinements. American Mineralogist, 83, 9-10.

Halenius, U., Skogby, H., and Andreozzi, G.B. (2002) Influence of cation distribution on the optical absorption spectra of Fe3+-bearing spinel s.s.-hercynite crystals: evidence for electron transitions in Fe-VI(2+)-Fe-VI(3+) clusters. Physics and Chemistry of Minerals, 29, 39-330.

Isaacson, P.J., Gillis-Davis, J.J., Jackson, C., Prissel, T.C., Parman, S., Donaldson Hanna, K., and Cheek, L. (2014), Experimental weathering of synthetic spinels, LPSC 45, #1612.

Karner, J.M., Sutton, S.R., Papike, J.J., Shearer, C.K., Jones, J.H., and Newville, M. (2006) Application of a new vanadium valence oxybarometer to basaltic glasses from the Earth, Moon, and Mars. American Mineralogist, 91, 270-277.

Kaur, P., Chauhan, P., Bhattacharya, S., Ajai, and Kumar, A.S.K. (2012) Compositional Diversity at Tycho Crater: Mg-Spinel Exposures Detected from Moon Mineralogy Mapper (M3) Data, p. Abstract# 1434, Lunar Planetary Science Conference.

Lal, D., Chauhan, P., Shah, R.D., Bhattacharya, S., Ajai, and Kumar, A.S.K. (2012) Detection of Mg spinel lithologies on central peak of crater Theophilus using Moon Mineralogy Mapper (M3) data from Chandrayaan-1. Journal of Earth System Science, 121, 847-853.

Mao, H.K., and Bell, P.M. (1975) Crystal-field effects in spinel: oxidation states of iron and chromium. Geochimica Et Cosmochimica Acta, 39, 865-866, IN1-IN2, 867-874.

McCallum, I.S., and O'Brien, H.E. (1996) Stratigraphy of the lunar highland crust: Depths of burial of lunar samples from cooling-rate studies. American Mineralogist, 81, 1166-1175.

Murphy, S.T., Gilbert, C.A., Smith, R., Mitchell, T.E., Grimes, R.W. (2010) Non-stoichiometry in $MgAl_2O_4$ spinel. Philosophical Magazine, 90:10, 1297-1305.

Murray R. W., Miller D. J. and Kryc K. A. (2000), Analysis of major and trace elements in rocks, sediments, and interstitial waters by Inductively Coupled Plasma-Atomic Emission Spectroscopy (ICP-AES). Texas A&M University, ODP Technical Note 29, 21 pp.

Navrotsky, A. , and Kleppa, O.J. (1967) Thermodynamics of cation distributions in simple spinels. Journal of Inorganic & Nuclear Chemistry, 29, 2701-2714.

O'Neill, H.S.C., and Navrotsky, A. (1983) Simple spinels; crystallographic parameters, cation radii, lattice energies, and cation distribution. American Mineralogist, 68, 181-194.

Pieters, C. M., E. M. Fischer, O. Rode, and A. Basu (1993) Optical effects of space weathering: The role of the finest fraction. Joournal of Geophysical Research, 98, 20,817-20,824.

Pieters, C.M., and T. Hiroi (2004) RELAB (Refectance Experiment Laboratory): A NASA Multiuser Spectroscopy Facility, *Lunar and Planetary Science Conference XXXV*, #1720.

Pieters, C.M., Besse, S., Boardman, J., Buratti, B., Cheek, L., Clark, R.N., Combe, J.P., Dhingra, D., Goswami, J.N., Green, R.O., Head, J.W., Isaacson, P., Klima, R., Kramer, G., Lundeen, S., Malaret, E., McCord, T., Mustard, J., Nettles, J., Petro, N., Runyon, C., Staid, M., Sunshine, J., Taylor, L.A., Thaisen, K., Tompkins, S., and Whitten, J. (2011) Mg-spinel lithology: A new rock type on the lunar farside. Journal of Geophysical Research-Planets, 116, E00G08

Pieters, C.M., Donaldson-Hanna, Kerri, Cheek, L, Dhingra, D, Prissel, T, Jackson, C, Moriarty, D, Parman, S, Taylor, L.A. The Distribution and Origin of Mg-Spinel on the Moon. Submitted to American Mineralogist, lunar highlands special issue

Prinz, M., Dowty, E., Keil, K., and Bunch, T.E. (1973) Spinel troctolite and anorthosite in Apollo 16 samples. Science, 179, 74-76.

Prissel, T.C., Parman, S.W., Jackson, C.R.M., Rutherford, M.J., Hess, P.C, Head, J.W., Cheek, L., Dhingra, D., Pieters, C.M.,Pink Moon: Lunar Melt-Rock Interactions & the Petrogenesis of Pink Spinel Anorthosites, Submitted to Earth and Planetary Sciences Letters

Redfern, S.A.T., Harrison, R.J., O'Neill, H.S.C., and Wood, D.R.R. (1999) Thermodynamics and kinetics of cation ordering in $MgAl_2O_4$ spinel up to 1600 ˚C from in situ neutron diffraction. American Mineralogist, 84, 299-310.

Ridley, W.I., Hubbard, N.J., Rhodes, J.M., Weismann, H., and Bansal, B. (1973) The Petrology of Lunar Breccia 15445 and Petrogenetic Implications. The Journal of Geology, 81, 621-631.

Saal, A.E., Hauri, E.H., Cascio, M.L., Van Orman, J.A., Rutherford, M.C., and Cooper, R.F. (2008) Volatile content of lunar volcanic glasses and the presence of water in the Moon's interior. Nature, 454, 192-195.

Sato, M., Hickling, N., and McLane, J.E. (1973) Oxygen fugacity values of Apollo 12, 14, and 15 lunar samples and reduced state of lunar magmas. Lunar and Planetary Science Conference Proceedings, 4, p. 1061.

Salisbury, J. W. and Walter, L. S. (1989) Thermal infrared (2.5 – 13.5 microns) spectroscopic remote sensing of igneous rock types on particulate planetary surfaces. Journal of Geophysical Research, 94, 9192-9202.

Salje, E. (1988) Kinetic rate laws as derived from order parameter theory I: Theoretical concepts. Physics and Chemistry of Minerals, 15, 336-348.

Schmalzried, H., *Solid State Reactions*, (2^{nd} edition), 254 pp., Verlag Chemie, Weinheim, FRG, 1981.

Skogby, H., Annersten, H., Domeneghetti, M.C., Molin, G., and Tazzoli, V. (1992) Iron distribution in orthopyroxene: A comparison of Mössbauer spectroscopy and X-ray refinement results. European journal of mineralogy, 4(3), 441-452.

Skogby, H., and Halenius, U. (2003) An FTIR study of tetrahedrally coordinated ferrous iron in the spinel-hercynite solid solution. American Mineralogist, 88(4).

Sunshine, J.M., Pieters, C.M., and Pratt, S.F. (1990) Deconvolution of mineral absorption bands: An improved approach. Journal of Geophysical Research: Solid Earth (1978–2012), 95(B5), 6955-6966.

Sunshine, J., Besse, S., Petro, N., Pieters, C., Head, J., Taylor, L., Klima, R., Isaacson, P., Boardman, J., and Clark, R. (2010) Hidden in plain sight: Spinel-rich deposits on the nearside of the Moon as revealed by Moon Mineralogy Mapper (M3). Lunar and Planetary Institute Science Conference Abstracts, 41, p. 1508.

Takeda, H., Miyamoto, M., Ishii, T., and Lofgren, G.E. (1975) Relative cooling rates of mare basalts at the Apollo 12 and 15 sites as estimated from pyroxene exsolution data, p. 987-996. Lunar Science Conference VI.

Taran, M.N., Koch-Muller, M., and Langer, K. (2005) Electronic absorption spectroscopy of natural (Fe2+, Fe3+)-bearing spinels of spinel s.s.-hercynite and gahnite-hercynite solid solutions at different temperatures and high-pressures. Physics and Chemistry of Minerals, 32, 175-188.

Vaughan, W.M., Head, J.W., Wilson, L., and Hess, P.C. (2013) Geology and petrology of enormous volumes of impact melt on the Moon: A case study of the Orientale basin impact melt sea. Icarus, 223(2), 749-765.

Watson, E.B., and Price, J.D. (2002) Kinetics of the reaction $MgO+Al_2O_3$ -> $MgAl_2O_4$ and Al-Mg interdiffusion in spinel at 1200 to 2000 ˚C and 1.0 to 4.0 GPa. Geochimica Et Cosmochimica Acta, 66, 2123-2138.

Yamamoto, S., Nakamura, R., Matsunaga, T., Ogawa, Y., Ishihara, Y., Morota, T., Hirata, N., Ohtake, M., Hiroi, T., and Yokota, Y. (2013) A new type of pyroclastic deposit on the Moon containing Fe-spinel and chromite. Geophysical Research Letters, 40, 4549-4554.

Yue, Z., Johnson, B., Minton, D., Melosh, H., Di, K., Hu, W., and Liu, Y. (2013) Projectile remnants in central peaks of lunar impact craters. Nature Geoscience, 6(6), 435-437.

Zhang, N., Parmentier, E., and Liang, Y. (2013) Effects of lunar cumulate mantle overturn and megaregolith on the expansion and contraction history of the Moon. Geophysical Research Letters, 40, 5019-5023.

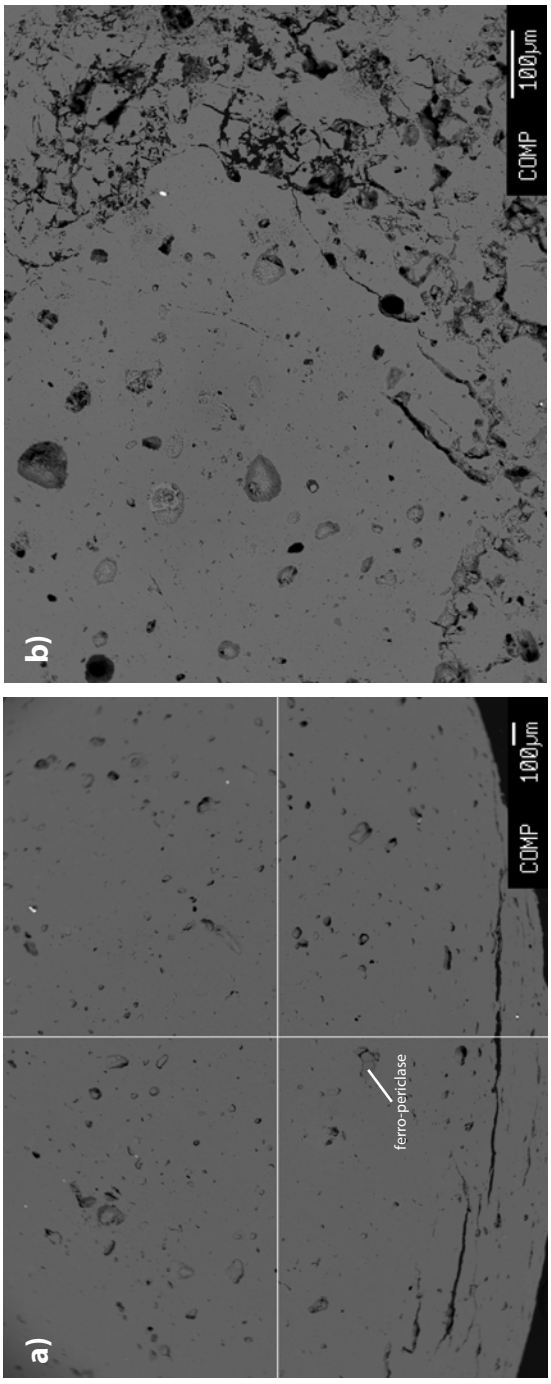

Figure 1

Figure 2

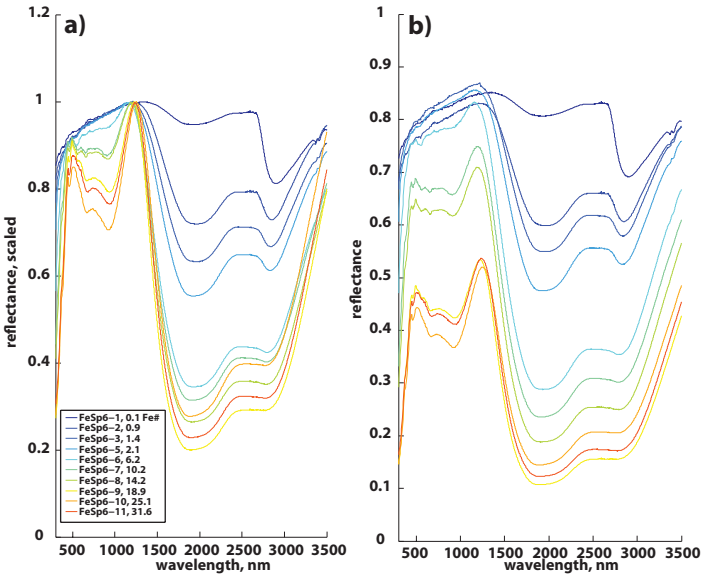
a)
b)
reflectance, scaled
reflectance
wavelength, nm
wavelength, nm
FeSp6–1, 0.1 Fe#
FeSp6–2, 0.9
FeSp6–3, 1.4
FeSp6–5, 2.1
FeSp6–6, 6.2
FeSp6–7, 10.2
FeSp6–8, 14.2
FeSp6–9, 18.9
FeSp6–10, 25.1
FeSp6–11, 31.6

Fig. 3

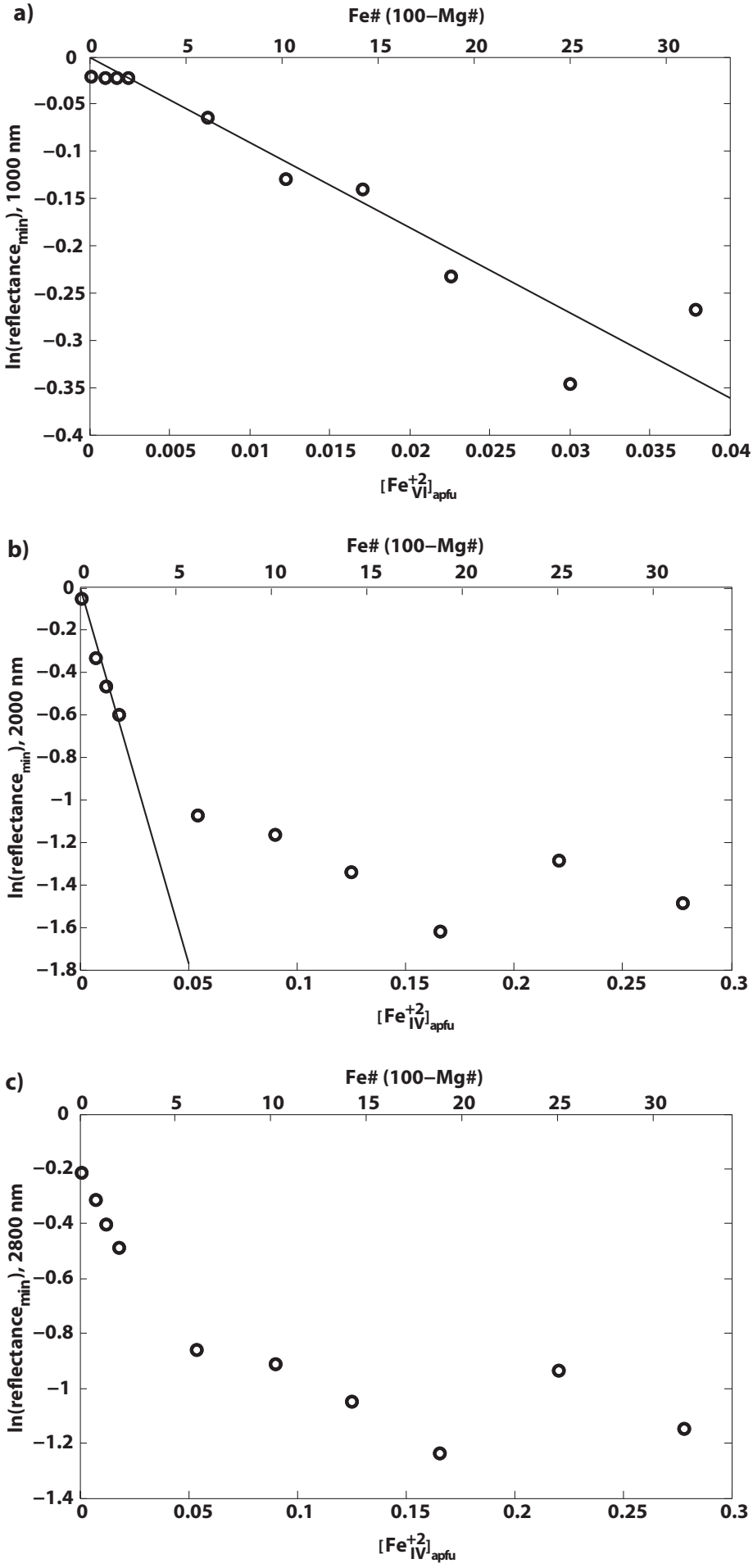
a)
Fe# (100–Mg#)
ln(reflectance$_{min}$), 1000 nm
[Fe$^{+2}_{VI}$]$_{apfu}$
b)
Fe# (100–Mg#)
ln(reflectance$_{min}$), 2000 nm
[Fe$^{+2}_{IV}$]$_{apfu}$
c)
Fe# (100–Mg#)
ln(reflectance$_{min}$), 2800 nm
[Fe$^{+2}_{IV}$]$_{apfu}$

Fig. 4

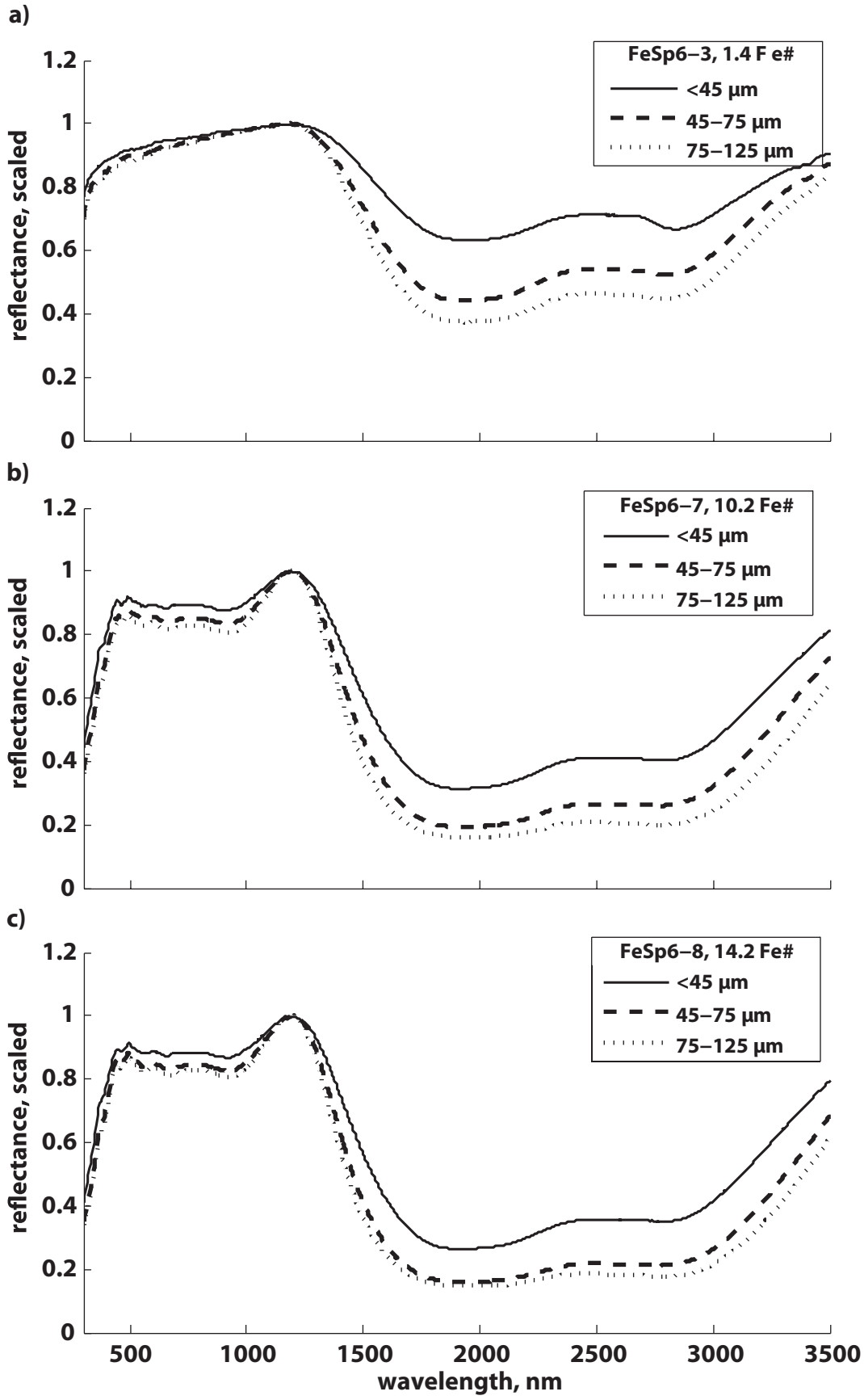
a)
FeSp6–3, 1.4 F e#
<45 µm
45–75 µm
75–125 µm
reflectance, scaled
b)
FeSp6–7, 10.2 Fe#
<45 µm
45–75 µm
75–125 µm
reflectance, scaled
c)
FeSp6–8, 14.2 Fe#
<45 µm
45–75 µm
75–125 µm
reflectance, scaled
0
0.2
0.4
0.6
0.8
1
1.2
500
1000
1500
2000
2500
3000
3500
wavelength, nm

Fig. 5

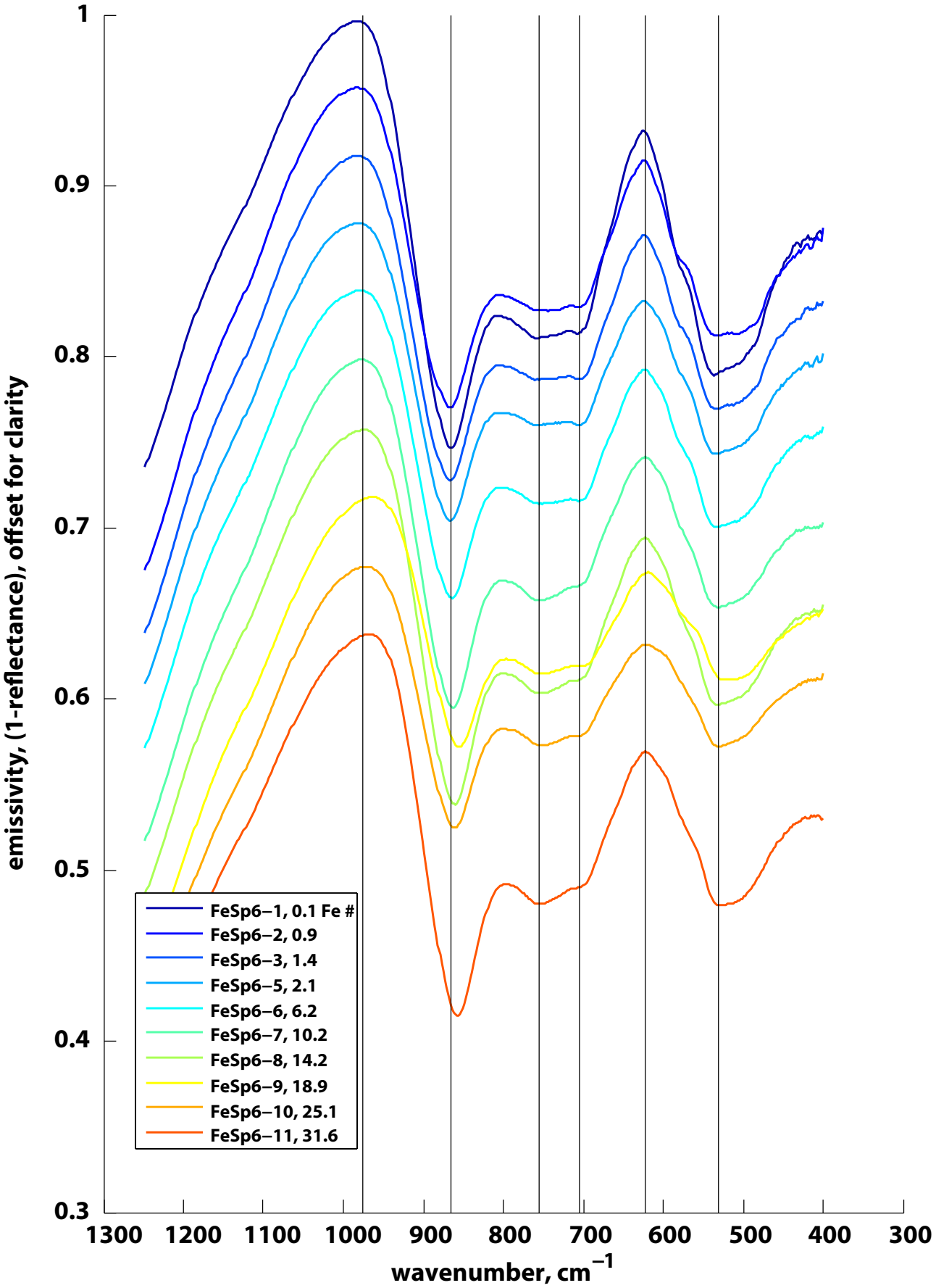
emissivity, (1-reflectance), offset for clarity
wavenumber, cm^{-1}
1
0.9
0.8
0.7
0.6
0.5
0.4
0.3
1300
1200
1100
1000
900
800
700
600
500
400
300
FeSp6–1, 0.1 Fe #
FeSp6–2, 0.9
FeSp6–3, 1.4
FeSp6–5, 2.1
FeSp6–6, 6.2
FeSp6–7, 10.2
FeSp6–8, 14.2
FeSp6–9, 18.9
FeSp6–10, 25.1
FeSp6–11, 31.6

Fig. 6

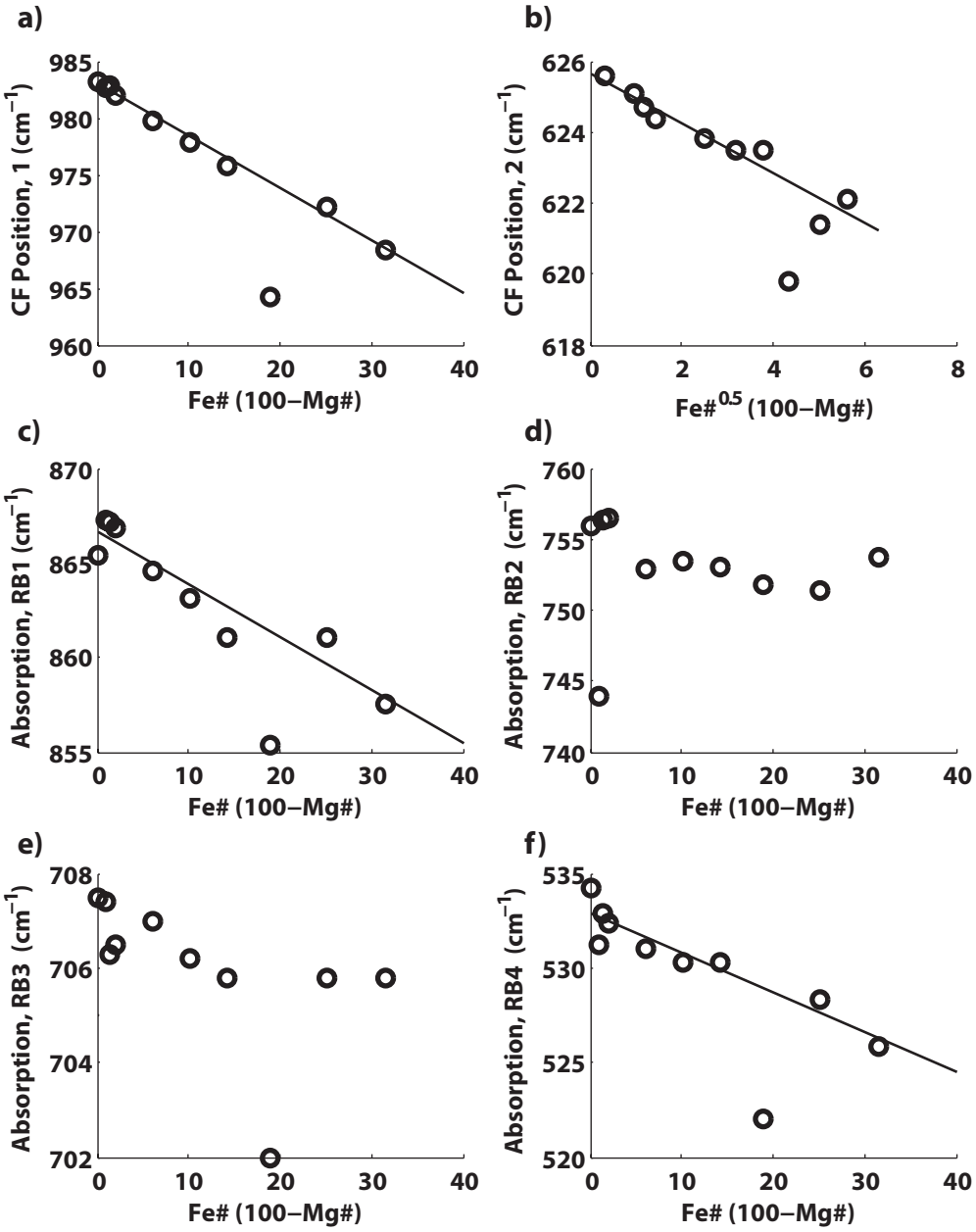
a)
CF Position, 1 (cm^{-1})
985
980
975
970
965
960
0
10
20
30
40
Fe# (100–Mg#)
b)
CF Position, 2 (cm^{-1})
626
624
622
620
618
0
2
4
6
8
Fe#$^{0.5}$ (100–Mg#)
c)
Absorption, RB1 (cm^{-1})
870
865
860
855
0
10
20
30
40
Fe# (100–Mg#)
d)
Absorption, RB2 (cm^{-1})
760
755
750
745
740
0
10
20
30
40
Fe# (100–Mg#)
e)
Absorption, RB3 (cm^{-1})
708
706
704
702
0
10
20
30
40
Fe# (100–Mg#)
f)
Absorption, RB4 (cm^{-1})
535
530
525
520
0
10
20
30
40
Fe# (100–Mg#)

Fig. 7

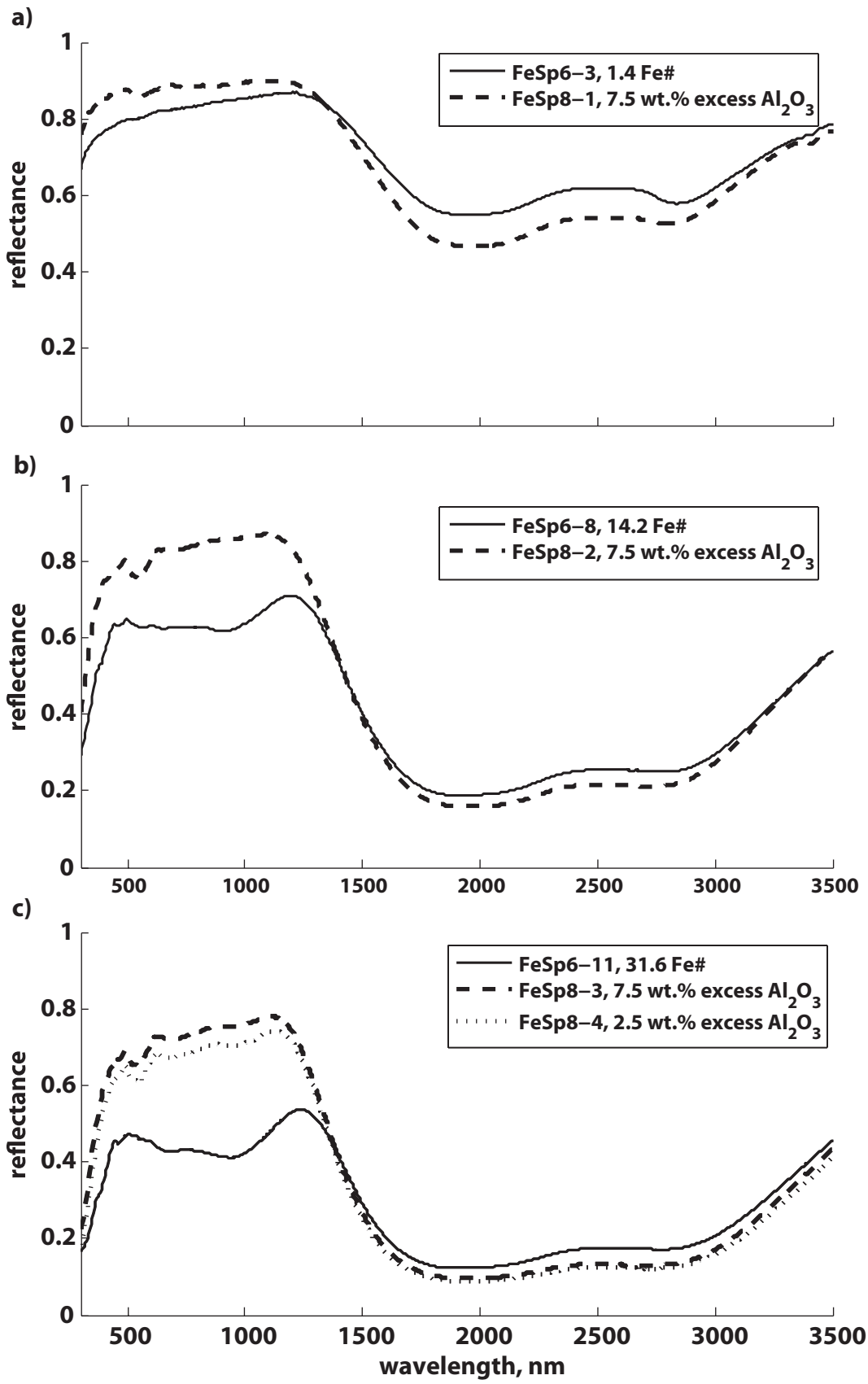
a)
b)
c)
reflectance
wavelength, nm
FeSp6–3, 1.4 Fe#
FeSp8–1, 7.5 wt.% excess Al2O3
FeSp6–8, 14.2 Fe#
FeSp8–2, 7.5 wt.% excess Al2O3
FeSp6–11, 31.6 Fe#
FeSp8–3, 7.5 wt.% excess Al2O3
FeSp8–4, 2.5 wt.% excess Al2O3
0
0.2
0.4
0.6
0.8
1
500
1000
1500
2000
2500
3000
3500

Fig. 8

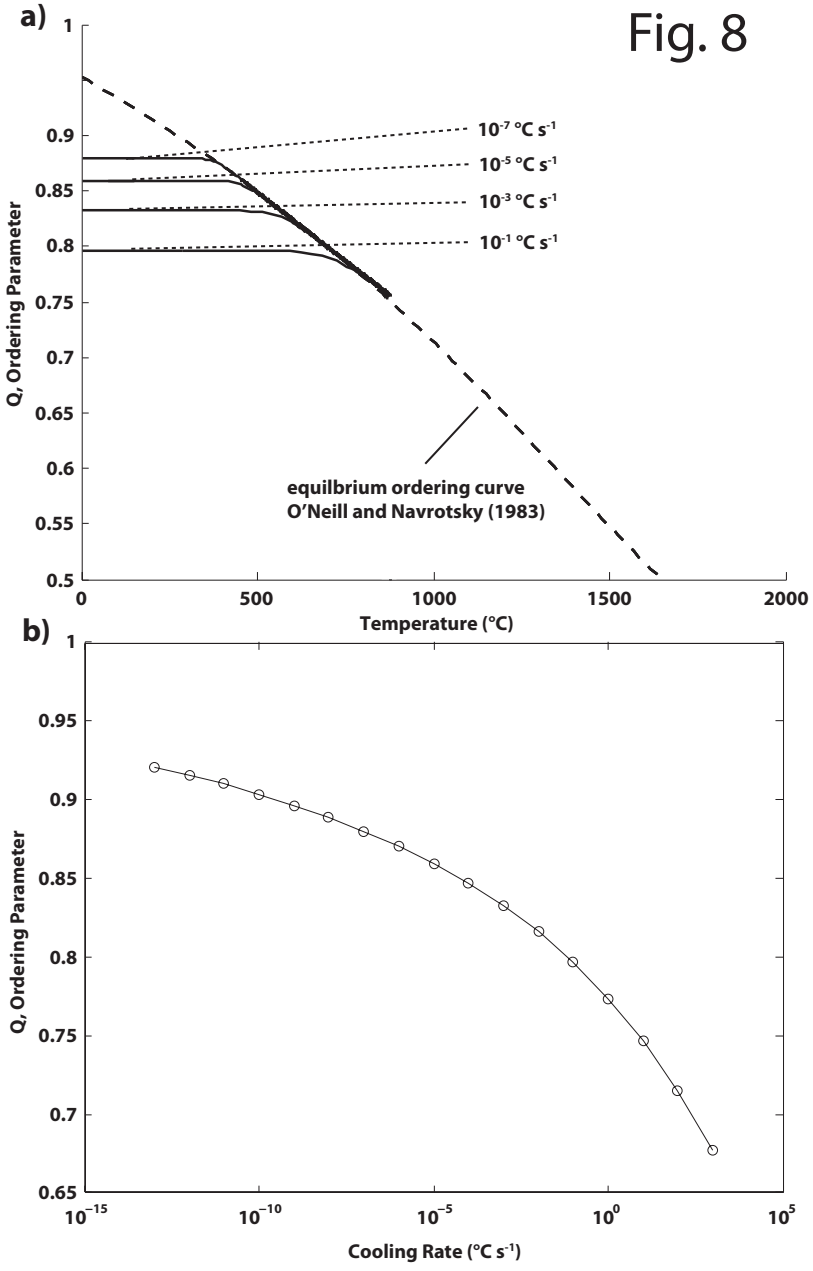
a)
Q, Ordering Parameter
Temperature (°C)
10-7 °C s-1
10-5 °C s-1
10-3 °C s-1
10-1 °C s-1
equilbrium ordering curve
O'Neill and Navrotsky (1983)
b)
Q, Ordering Parameter
Cooling Rate (°C s-1)